

Bachelor Thesis: Magnetic shielding in SAFARI

*Technische Natuurkunde (HHS) / Technical Physics (The Hague
University of Applied Sciences)*

28 August – 19 December 2013

By: Kevin Ravensberg

Supervisors SRON: Henk van Weers, Luciano Gottardi, Jan van der Kuur

Supervisors HHS: P. Menger, L.H. Arntzen



Abstract:

Research is done on the properties of a niobium superconducting magnetic shield sample (see image below this abstract), its magnetic attenuation; and behaviour around the transition temperature 9.25 K. The attenuation of the magnetic shield sample was measured in a cryogenic setup. This is required to verify that the TES bolometers will not measure any magnetic signals as noise when shielded. A new in-field cooling technique was experimentally investigated with measurements during superconductivity phase-transitions. Cooling the shield from a single point could in theory allow the expulsion of a remnant magnetic field.

Previous work on this project showed a deviation in measured and modelled attenuation. Both the measurement and model have been refined during this thesis. They are now in agreement within the significance of the measured data points until a certain depth in the shield sample.

It is known that type II superconductors have a mixed Meissner state at the start of the phase transition. This causes the trapping of a magnetic field inside the superconductor. Measurements using the progression controlled cooling technique showed a reduction of 60~100% for the remnant magnetic field (only in the bottom part of the sample) present during cooling. This was not repeatable for fields of order 10 μ T generated by a solenoid.

Concluding that required attenuation of $A^{-1} = 10^{-5}$ in the z-direction has been verified for the shield sample at the supposed detector position. This was measured down to $A^{-1} \cong 10^{-6}$ at the lowest measurable depth in this sample. Experimental evidence was found to support the viability of the suggested in-field cooling technique, but only for remnant magnetic fields in the order of ~100 nT.



Index

List of abbreviations	5
1 Introduction	6
1.1 Stichting Ruimte Onderzoek Nederland*	6
1.2 Science case SPICA	6
1.3 SAFARI	7
1.4 Research assignment.....	8
1.4.1 Motivation.....	8
1.4.2 Research question I:	8
1.4.3 Research question II:	9
1.4.4 Solution strategy	9
2 Measurement strategy.....	9
3 Magnetic shielding and superconductivity.....	9
3.1 Magnetism and Matter.....	9
3.1.1 Superconductivity	10
3.1.2 Topological flux trapping	12
3.1.3 Non-topological flux trapping (in Abrikosov vortices)	13
3.2 Generators of magnetic fields.....	13
3.2.1 Magnetic field generated by a Solenoid.....	14
3.2.2 Magnetic Field generated by a Helmholtz coil	14
3.3 Attenuation of magnetic flux	15
3.4 Open cylinder attenuation model.....	16
3.5 Finite element model for magnetic attenuation	17
3.6 Magnetometer theory	18
3.6.1 dc-SQUID magnetometer.....	18
3.6.2 Fluxgate magnetometer (cryogenic)	20
3.6.1 Measuring flux density vector B.....	20
3.6.2 Error analysis	21
4 Experiments	22
4.1 Attenuation measuring setup.....	22
4.1.1 Insert.....	22
4.1.2 Dipstick	23
4.1.3 XYZ Reference coordinate frame	24
4.1.4 Solenoid Amplifier Circuit	26
4.1.5 Fluxgate calibration setup	26
4.2 Phase-transition trapping Experiment.....	27

4.2.1	Setup	27
4.3	In-field cooling Experiment	28
4.3.1	Modified setup.....	28
5	Summarized Results/ Additional Data Analysis	29
5.1	Closed Nb shield attenuation.....	29
5.1.1	2D COMSOL model analysis.....	30
5.1.2	3D Model analysis	31
5.2	Opened Nb shield attenuation	32
5.3	*2-part Nb shield attenuation	33
5.4	*Cryoperm shield attenuation	33
5.5	Superconduction-phase transition	34
6	Conclusion	36
	References.....	37
	Figure list:.....	38
7	Appendix A: Technical designs.....	40
7.1	Insert with solenoid.....	40
7.2	Insert with Nb closed shield.....	41
7.3	Nb shield with Fluxgate sensors	42
7.4	Point cooling (modification)	43
8	Appendix B: Measurement reports	44
8.1	Helmholtz x and y axis B profile.....	45
8.1.1	Method	45
8.1.2	Result.....	45
8.2	Fluxgate sensor characterization.....	45
8.2.1	Method	45
8.2.2	Result.....	46
8.3	dc-SQUID (3d-SQUID) amplified response & noise level.....	46
8.3.1	Method	46
8.3.2	Result.....	47
8.3.3	RF-noise from nearby sources	48
8.4	SQUID rotation around x-axis.....	48
8.4.1	Method	48
8.4.2	Result.....	48
8.5	Low frequent AC solenoid flux.....	50
8.5.1	Method	50
8.5.2	Result.....	50

8.6	Solenoid dc-flux.....	51
8.6.1	Method	51
8.6.2	Result.....	51
8.7	Measured flux density as a function of fluxgate position	52
8.7.1	Method	52
8.7.2	Result.....	52
8.8	Measured flux density as a function of SQUID height.....	53
8.8.1	Method	53
8.8.2	Result.....	53
8.9	Shield's magnetic attenuation.....	55
8.9.1	Method	55
8.9.2	Result.....	55
8.10	Residual magnetic field vectors	57
8.10.1	Method 1	57
8.10.2	Result.....	57
8.10.3	Method 2	58
8.11	Trapped magnetic field vectors	58
8.11.1	Method	58
8.11.2	Results	59
8.12	Phase transition (Meissner state) measurements	60
8.12.1	Method	60
8.12.1	Result.....	60
8.13	Point Cooled Phase-transition Experiment	64
8.13.1	Method	64
8.13.2	Result.....	64
9	Appendix C: Calibration parameters	66
9.1	(cryo-)Solenoid.....	66
9.2	'3D' SQUID probe/dipstick.....	66
9.3	Fluxgate magnetometer	66
9.4	Helmholtz Setup.....	66
9.5	*Cooling down the Kelvinox II (cryostat)	67
9.6	*Placing the Insert (holder for the probe) with sliding seal	67
9.7	*Lowering dipstick with rotatable SQUID	67

List of abbreviations

In approximate order of appearance in this thesis.

Abbreviation	Expanded	Description
SRON	<i>Stichting Ruimte Onderzoek Nederland</i>	Place of research for this thesis.
SR&T	Sensor research and technology	Department of research project in SRON.
SPICA	Space infrared telescope for cosmology and astrophysics	Future infrared mission from JAXA/ESA.
JAXA	Japanese aerospace exploration agency	Lead agency in SPICA mission.
ESA	European space agency	Co-agency in SPICA mission.
NWO	<i>Nederlandse Organisatie voor Wetenschappelijk Onderzoek</i>	Organisation for scientific research in the Netherlands.
SAFARI	Spica far infrared instrument	Instrument contribution from SRON for SPICA mission.
ATHENA	Advanced telescope for high energy astrophysics	Future x-ray mission from ESA.
TES	Transition edge sensor	Superconducting detector, here used as a bolometer for photons.
SQUID	Superconducting quantum interference device	A device used as a magnetometer at low temperatures.
He	Helium	Coolant in cryostat.
Nb	Niobium	Material used for manufacturing magnetic shield, can become superconducting.
FEM	Finite element model	A computable model used for solving equations in physics problems.

1 Introduction

First a short introduction is given into the overarching project SAFARI at SRON of which the magnetic shielding is a subproject, secondly the purpose of this research and the specific research questions will be given in Ch. 1.4.

1.1 Stichting Ruimte Onderzoek Nederland* (Netherlands Institute for Space Research)

As a space research institute collaborations with other institutes and agencies worldwide are needed to build the next great observatories of the future, ESA and JAXA are the space agency's cooperating on the future SPICA mission.



Figure 1. Logos of SPICA mission and SAFARI project.

The goal of SRON is to provide: *'the ensemble of knowledge and skills, both technically and scientifically, required to perform a principal role in the scientific utilization of space.'* (see reference: [i]) This includes research and development of new enabling technologies at the division SR&T, where the technology is matched to the scientific requirements to answer scientific questions (see Ch. 1.2 for examples). The *magnetic shielding* project is part of the experimental research done for enabling technology, potentially reducing shielding weight in flight. SRON is funded by the NWO and several smaller research budgets.

1.2 Science case SPICA

With the SPICA satellite (far)-red shifted (210~34 μm spectral bandwidth) galaxies could be imaged with the background radiation being the limiting noise factor (order 10^2 better than predecessor Herschel), this requires an 3.05 m effective diameter focal mirror cooled down to several Kelvin and a sensitive (well shielded) detector array.

The big science questions this mission [ii] aims to answer are:

- How do stars and galaxies form and evolve over cosmic time?

Are black holes the seeds for the galaxies in our universe, or were they formed in already existing young galaxies?; What types of galaxies were present in the 'early' visible universe?; ... and any question the answers to these questions will raise.

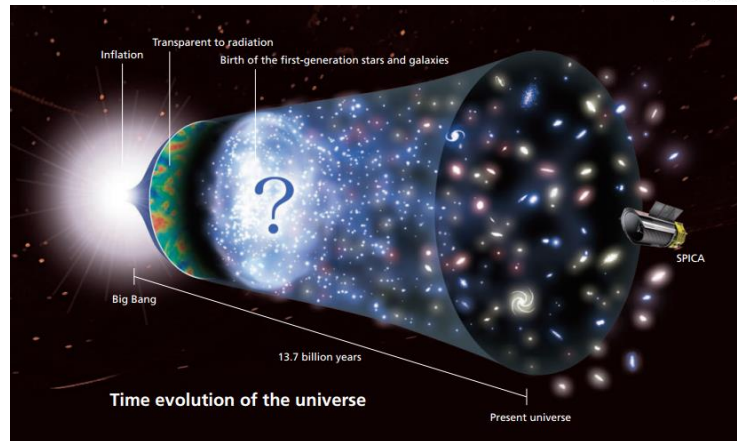


Figure 2. Mission illustration from SPICA pamphlet (JAXA).

- How does our solar system relate to other planetary systems and could life evolve elsewhere?

What processes take place from proto-planetary to debris disks in newly forming solar systems? Which molecules play important roles in the formation of planets?

1.3 SAFARI

In the FIR(Far Infra-Red 30~210 μm) imager SAFARI (Spica FAR-infrared Instrument) there is a magnetic shield designed to keep magnetic influences away from the magnetic noise sensitive TES bolometer array.

Figure 3 illustrates an engineering model of a TES array suspended inside cooled/shielded suspension. The photons enter through the aperture at the top to fall on the TES array that is magnetically shielded by a combination of Cryoperm and niobium layers. The niobium shield is held in place by thin thermally isolating wires in order to keep the TES sensor array at temperatures of 50 mK.

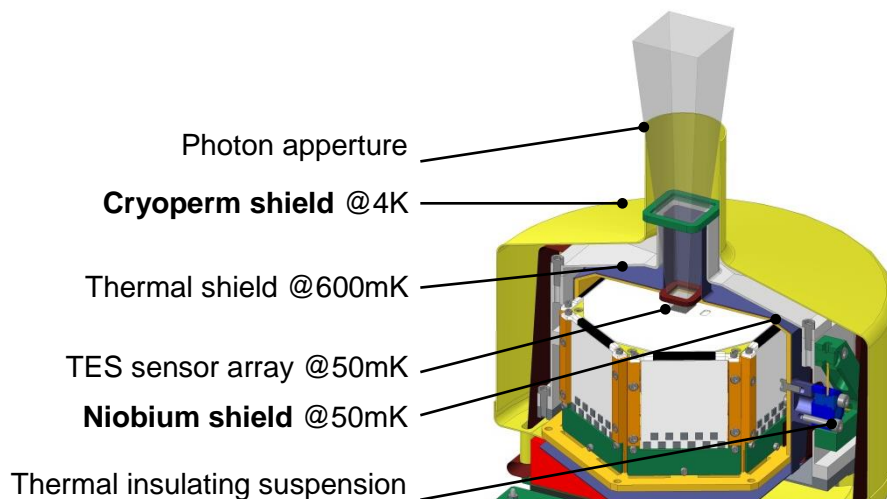


Figure 3. Illustration of magnetically and thermally shielded TES sensor array, made by: Henk van Weers

It is known that thermal noise is an issue in high resolution infrared spectroscopy. It is due to the infrared noise emitted from the instrument itself. This warm body radiation is reduced by cooling the mirror (6K), detectors and the thermal shield surrounding the inner layers of the

sensor. Next to this the TES is also sensitive to magnetic field fluctuations and its sensitivity benefits from a nulled field, this is the reason to use a superconducting niobium shield layer. A *ferromagnetic* spherical shield with high permeability has an attenuation that is proportional to the shield thickness and inversely proportional to its radius. A superconductor only needs a thickness of several times the London penetration depth (~ 70 nm for Nb) for its maximum attenuation.

The requirement for this magnetic shielding in SAFARI is to reduce the magnetic flux density at the TES detector to a factor ($B_{attenuated}/B_{noise}$) $< 1 \cdot 10^{-4}$ of the flux density present without shielding, see Ch. 3.3 for the definition of this shielding factor. Similar shielding designs for the ATHENA mission would require a higher shielding factor of $1 \cdot 10^5 \rightarrow 1 \cdot 10^6$ depending on the chosen detector.

1.4 Research assignment

For this thesis the magnetic field attenuation of a niobium shield sample is measured. The magnetic field left inside a superconductive shield depends on the field present during cooling, this is referred to as flux trapping. A technique for in-field cooling [ix] theoretically showed a possible expulsion of the trapped flux. Measurements have been done to investigate the effect of this technique applied on the niobium shield sample.

1.4.1 Motivation

The purpose of this research is to validate the magnetic attenuation factor requirement from the SAFARI project on the shielding samples at SRON. This is done by several measurements of the attenuation and an investigation of the behaviour of the shielding during the transition to superconductivity.

The further experimental investigation of Nb through its superconducting phase transition is motivated by the theory of 'progression controlled cooling' [ix]. This technology would allow to expel the remnant magnetic field from the inside of a superconducting magnetic shield, by exploiting the Meissner effect in superconductor material.

Next the main research questions following from the motivation are given and described.

1.4.2 Research question I:

The problem of an unshielded TES array is a varying sensitivity (or noise signal) as a function of the magnetic field, the specific effects on various detector parameters are described by [iii]. This is solved by attenuating the magnetic field many orders of magnitude. So the first research question following from this problem is:

What is the magnetic attenuation of the superconducting Nb shield?

Previous attenuation measurements have shown that a model for a cylindrical shield fitted lab measurements, but a more complex shield design showed two significant deviations from the modelled magnetic shield.

During this thesis an explanation for this deviation is sought, by measurements with a more sensitive magnetometer (SQUID). This SQUID will first be characterised and calibrated on its absolute sensitivity and measuring range.

1.4.3 Research question II:

Depending on the magnetic environment of the superconducting shield during the phase transition a different field magnitude and direction could be left at the detector area. This leads to the following question:

How does the Nb shield behave around the superconducting phase transition and how will it trap an external magnetic field present at the transition?

The behaviour of superconducting materials around their transition temperature is not well understood, this is investigated by experiments with a niobium shield sample using SQUID- and fluxgate magnetometers. The purpose of this experiment is the proof of concept for an in-field cooling technique suggested (by [ix]) for the ATHENA/SAFARI projects at SRON.

1.4.4 Solution strategy

The theory of the interaction between superconductivity with magnetism is investigated (by literature study) to understand the physical principles observed in the experiments. Measurements of the magnetic attenuation are done with calibrated equipment. An experiment setup is constructed to investigate the behaviour of the niobium (a type II superconductor) shield sample around the phase transition.

2 Measurement strategy

To determine the magnetic attenuation of the Nb magnetic shield sample.

Before measurements can be done, the magnetometer should be tested on functionality. Only after calibrating both the magnetometer and electrical/mechanical setup, reproducible measurements of the magnetic attenuation can be done inside the cryostat/Dewar. The measurement reports for this thesis are found in Appendix B: Measurement reports.

The first result that should be acquired by these measurements is the attenuation profile along the z-direction inside the shield sample. This profile can be compared with the attenuation profile modelled for previous work in this project.

Secondly an experiment will be setup for measuring an indication of flux expulsion due to the Meissner effect in the shield sample. This should be a proof of concept measurement for the suggested in-field cooling method.

3 Magnetic shielding and superconductivity

In this chapter the models and theories of magnetic attenuation or the shielding factor, type II superconductors, flux trapping and finite element modelling of these phenomena are described. These theories allow to explain (and modelling of) the physical nature of the conducted experiments and to draw conclusions from the experiment results. Fundamentally magnetism is understood to be about electron spin alignment (magnetisation) where superconductivity is the forming of electron pairs (also called Cooper pairs) in a material.

3.1 Magnetism and Matter

The magnetic force is a phenomenon that affects moving charged particles (also electric currents). A magnetic field describes this exerted force component on a moving charge at

each point in space. In ordinary matter only magnetic dipoles have been found to exist, causing all of the field lines to close in on themselves in a limited area creating loops as illustrated in Figure 4.

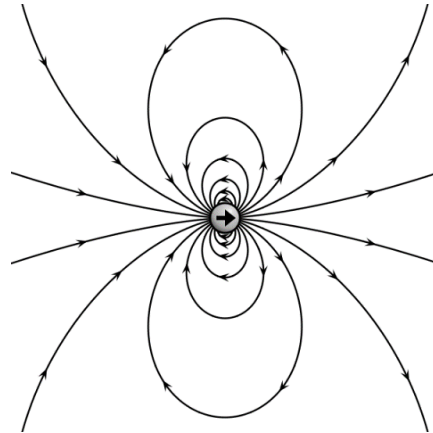


Figure 4. Illustration of a dipole, arrows indicate the direction of the field along the field line, source(http://en.wikipedia.org/wiki/File:VFpt_dipole_point.svg).

Magnetic flux can be seen as the density of magnetic field lines through a certain volume or area, a higher magnetic flux density B (T or Wb/m²) can exert a greater force on a charged particle moving through that flux density.

Magnetic fields are affected by the presence of matter, which can be divided into para-, ferro- or dia-magnetic materials. Paramagnetic materials are attracted to higher magnetic flux densities in space. Ferromagnetic materials can be magnetized, aligning its Weiss domains in the direction of magnetization. Diamagnetic materials are repelled from higher magnetic flux densities, although the force on diamagnetic materials is in general many orders of magnitude smaller than the force on ferromagnetic materials. Ideal type I superconductors appear to be perfectly diamagnetic, but have a more complex relation with magnetic fields than expected from perfect conductors. This property makes superconductive materials ideal (best shielding / mass ratio) to use as magnetic shielding in a space mission.

3.1.1 Superconductivity

Superconductive (type I) material has 2 properties that are different from regular conducting material, first is the ideal conductivity (no electron/ ion friction) of electricity with resistance $\rho = 0 \Omega$ instead of $\rho = \rho_0$, see Figure 5 for the relation of resistivity ρ with temperature T . Second is the Meissner effect, showing complete expulsion of all magnetic field lines from the superconductor. This only lasts until the magnetic field is high enough to break up the Cooper pairs that formed in the electron/ ion lattice. A Cooper pair is made of two electrons at a distance of ~ 100 nm (known as the coherence length) from each other in a lattice of ions. As the ions are slightly attracted to one electron, locally a slightly positively charged region is created. The other electron is attracted to this region to cancel out the slight positive charge. If a material is cold enough (not enough vibrational energy) then the bond between these electron pairs is unable to be broken by lattice vibrations (phonons), explaining the concept of frictionless movement of Cooper pairs (or currents) in a superconductor.

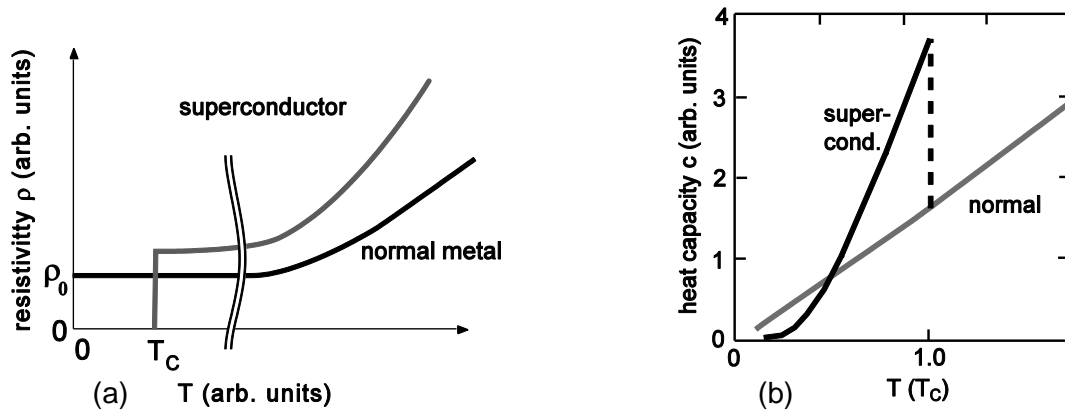


Figure 5. Illustration of (a) resistivity, (b) heat capacity, as a function of temperature comparing super- to conventional conductor material, source (<http://users-phys.au.dk/philip/pictures/physicsfigures/>).

A superconductor is theoretically characterized by 2 physical parameters (illustrated in Figure 6) in the Ginzburg-Landau theory:

- London magnetic field penetration depth, λ , (1)
- Superconducting coherence length, ξ , (2)

where the coherence length is given for a superconductor below the critical temperature.

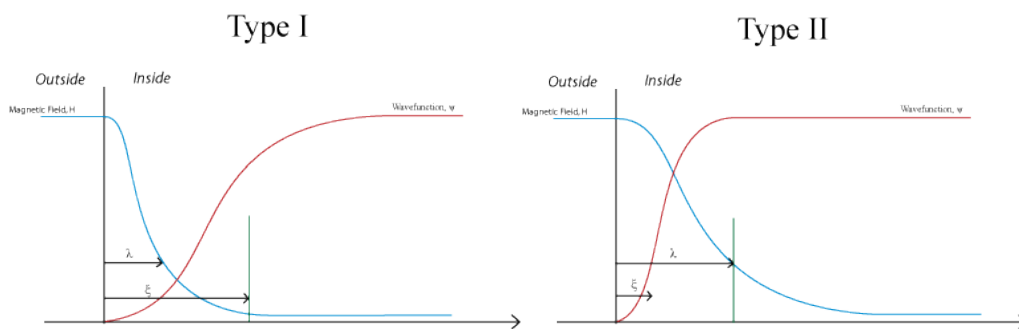


Figure 6. Illustration of magnetic field penetration depth inside superconductors (type I & II), source: (<http://www.doitpoms.ac.uk/tlplib/superconductivity/type.php>)

The magnetic field (of B_0 parallel to the surface) follows an exponential decay along the distance x in the superconductor, as in equation (3) (given by [14]):

$$B(x) = B_0 e^{-x/\lambda}, \quad (3)$$

A simplified (for an infinitely long/wide superconducting wall, in a homogeneous field) calculation of the required thickness to attenuate by 6 orders in magnitude for $\lambda = 39 \cdot 10^{-9}$ m (niobium) gives $\sim 5.4 \mu\text{m}$, which is remarkably thin for this order of attenuation compared to μ -metals. In finite shaped superconductors the required Lenz shielding currents to expel the magnetic field might exceed the critical current density J .

From the ratio $\kappa = \lambda/\xi$, between the penetration depth λ and coherence length ξ (38 nm for niobium) respectively, the critical magnetic field is given as:

$$B_{c1} \propto \ln(\kappa)/\kappa, \quad (4)$$

for the lower critical field and:

$$B_{c2} \propto \kappa, \quad (5)$$

for the upper critical field with $\kappa > \sqrt{2}$. Where below B_{c1} the material acts like a perfect superconductor and between B_{c1} and B_{c2} there is a special state that is specific for type II superconductors. Here the magnetic field can locally be strong enough to break the Cooper pair bond (by torque from the magnetic moment), allowing a flux vortex surrounded by shielding currents to pass through the superconductive material. In Figure 7 the temperature dependence of these critical magnetic fields are illustrated relative to critical temperature T_c . For a higher magnetic field, a lower temperature is required to observe flux expulsion by the Meissner effect.

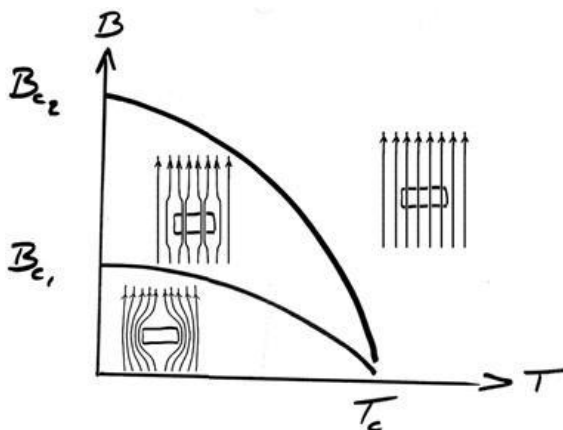


Figure 7. Illustration of type II superconductor state diagram, source: (<http://www.supraconductivite.fr/en/index.php?p=supra-levitation-phase-more>)

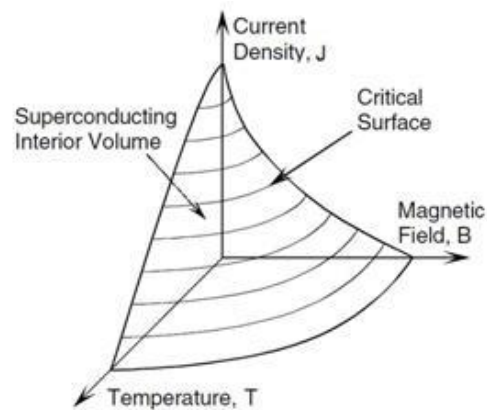


Figure 8. Illustration of superconductive state as a function of magnetic field B, current density J and temperature T, source: (<http://www.lhc-closer.es/1/4/8/0>).

There also is a critical super current-density J_c through a superconductor, above which the material returns to the normal state, illustrated in Figure 8. At edges in an arbitrary geometry, a higher current density could be required for the expulsion of the magnetic field. The *Bean critical state* model gives an approximation to the observed effects in superconductors from current-densities.

The geometry (topology) of a superconductor can cause the expelled flux to be trapped in a hole in the material. The mixed Meissner state does not depend on the geometry (non-topological).

3.1.2 Topological flux trapping

Multiple connected body (3D object with at least one hole) shaped superconductors are not always able to create a current density distribution in a way that cancels all magnetic flux from entering the volume inside the superconductor. Take the example (from Ch. 3.4) of an open cylinder that is able to attenuate the axially applied field more than the radially applied field demonstrates this, as the shape of a cylinder can function as a solenoid by providing an opposite field at lower current densities through the material for axial fields.

This also means that a magnetic field present during the superconductivity transition at T_c will be trapped more efficiently for an axial field rather than a radial applied field. Note that the magnetic flux lines are still completely expelled from the superconducting material (by the

Meissner effect) in topological trapping. The efficiency of trapping magnetic flux (present during $T_1 > T_c \rightarrow T_2 < T_c$) has been measured to be very high (~100%) and repeatable by [v].

3.1.3 Non-topological flux trapping (in Abrikosov vortices)

If a magnetic field B in the range $B_{c1} < B < B_{c2}$ is applied on a type II superconductor, then it is energetically preferable for the superconductor to allow a vortex of flux through superconducting wall in steps of ϕ_0 the magnetic flux quanta. This will happen at multiple places in the wall in a triangular lattice with a radius spacing approximately given by [vi]:

$$a \sim \sqrt{\phi_0/B}, \quad (6)$$

where:

a is the radius spacing, (m)

ϕ_0 is the flux quanta ($\frac{h}{2e}$). (Wb)

For Niobium the upper critical field B_{c2} has been measured by [vii] to be in the order of ~1 T (at ~5 K), depending on temperature and material purity. However there is actually a critical surface, along the temperature, magnetic field and current density variables present at the superconductor. For niobium (or other type II superconductor) a magnetic field present during the transition will first form a vortices lattice and then proceed to expel all magnetic flux due to the Meissner effect. Also more disorderly structures have been observed [viii], a collection of both can be seen in Figure 9.



Figure 9. (a) Magneto-optical, (b) magnetic force microscope, imaged vortices in a type II superconductor where bright dots are high flux densities at the superconductor surface, source: (<http://www.mn.uio.no/fysikk/english/research/groups/amks/superconductivity/vortex/index.html>).

As can be seen in Figure 7 when cooling the superconductor the magnetic field lines will first go through the vortex state and then to the Meissner state, a method to reduce the field trapped inside the superconductor by passing through the vortex state was suggested by [ix]. Here the shield should be cooled down from a single point on the body with a sufficient temperature gradient to allow the expulsion of most magnetic field lines from the shield. An experiment was done to investigate this non-topological trapping phenomenon, which is described in measurement report 8.12 in Appendix B: Measurement reports.

3.2 Generators of magnetic fields

During the experiments several magnetic field sources have been used, where earth's magnetic field can be assumed to be homogeneous in a space with no ferromagnetic material, the fields generated by finite coils are only approximately homogeneous in a limited volume. The magnetic flux density profiles can be modelled from faraday's law, for currents through copper wire coils.

3.2.1 Magnetic field generated by a Solenoid

By approximation the (axial) magnetic flux density produced by a solenoid (infinitely long) is given by equation (7):

$$B = \frac{\mu_r \mu_0 N I}{L}. \quad (7)$$

For any solenoid with a given amount N of loops on a length L with radius r the magnitude of magnetic flux density B at any position Z along the z -axis for a current I through the solenoid is approximately given by equation (8):

$$B(z) = \frac{\mu_r \mu_0 N I}{2L} r^2 \left(\frac{z + \frac{L}{2}}{\sqrt{\left(z + \frac{L}{2}\right)^2 + r^2}} - \frac{z - \frac{L}{2}}{\sqrt{\left(z - \frac{L}{2}\right)^2 + r^2}} \right), \quad (8)$$

where:

- L, r, z are length, radius and distance from centre, (m)
- I is the current through the wire, (A)
- $\mu_0 = 4\pi \cdot 10^{-7}$ (T/A)
- μ_r is the relative permeability. (-)

The direction of the magnetic field depends on the direction of the current, using the right hand rule (current along thumb, fingers curl in direction of the field) this can be deduced.

An electromagnetics simulation of the finite solenoid used would look like Figure 10, where all the field lines are actually closed loops going around the current carrying wire loops.

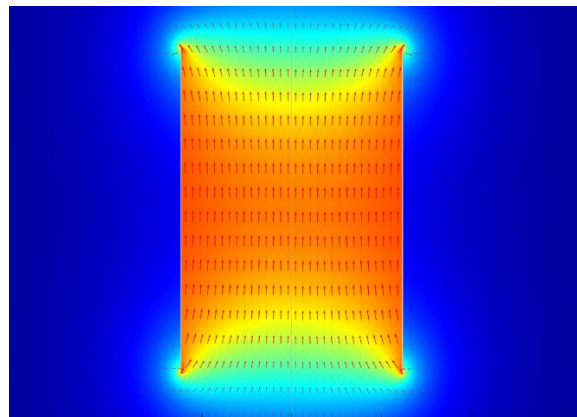


Figure 10. Illustration (from COMSOL) of magnetic flux density as color (blue=low to red=high) and arrow length, direction of the field is indicated by the direction of the red arrows.

The flux density profile along the vertical centre of the simulation would be analytically described by equation (8). The arrows drawn indicate the magnetic north (S→N inside, N→S outside solenoid).

3.2.2 Magnetic Field generated by a Helmholtz coil

A common method to produce an approximately homogenous field is to use a Helmholtz coil. The magnetic field magnitude and direction is approximately given by equation:

$$B = \left(\frac{4}{5}\right)^{\frac{3}{2}} \frac{\mu_r \mu_0 N I}{R}, \quad (9)$$

where:

B is the homogenous magnetic flux density at the centre, (T)
 I is the current through both coils, (A)
 R is the radius of the 2 coils, and distance between the coils, (m)
 N is the number of loops per coil, (-)
 $\mu_r \mu_0$ is the magnetic permeability of medium in centre. (T/A)

When the direction has to be variable, a second Helmholtz coil can be placed around the first, this setup has a total of 4 regular coils at 2 specific radii. A COMSOL model was made for this setup's geometry and the result is presented in Figure 11.

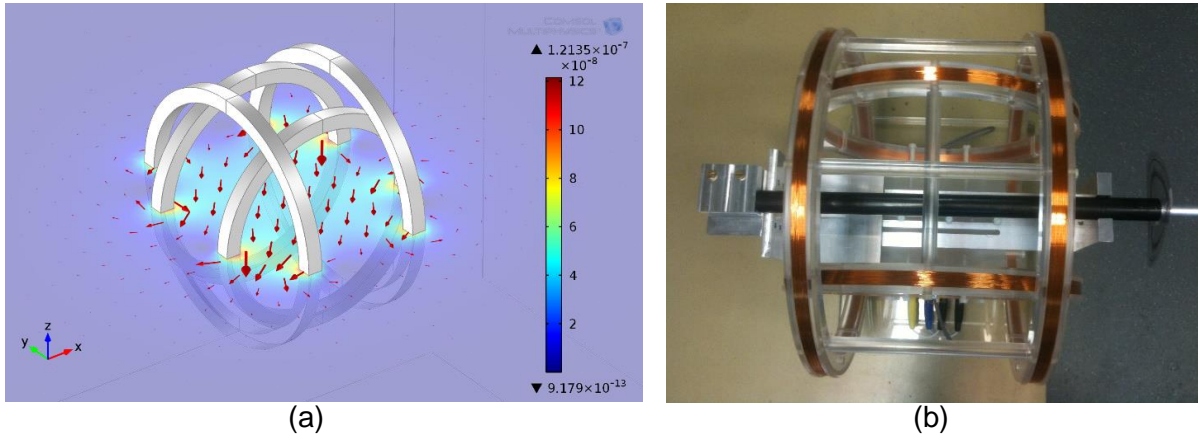


Figure 11. Model (a) of dual Helmholtz coil setup (b), demonstrating homogenous field at centre of the xy-plane.

If both x and y axial Helmholtz coils carry a certain current to generate a B_x and B_y according to equation (9), the resulting magnetic field amplitude is given as:

$$|B_{xy}| = \sqrt{B_x^2 + B_y^2}, \quad (10)$$

with angle θ_{xy} on the xy -plane (counter clockwise from the positive x -axis) of this field is given by equation:

$$\theta_{xy} = \tan^{-1}(B_y/B_x). \quad (11)$$

3.3 Attenuation of magnetic flux

A measure of how well a (generated) magnetic field is diverted from the shielded volume by the magnetic shield is given by its shielding factor. The definition of the shielding factor S is given as: $S = B_{applied}/B_{measured}$, thus a higher shielding factor results in a lower measured field at constant $B_{applied}$. Attenuation A is a more general synonym in physics to this shielding factor S used in literature of attenuation by a superconducting shield. In this thesis the relative measured flux density inside the magnetic shield $B_{measured}/B_{applied}$ is referred to as the inverse of attenuation A^{-1} .

3.4 Open cylinder attenuation model

The remnant fraction of $B_{applied}$ inside the open cylinder, see Figure 12, is called the attenuated flux $B_{attenuated}$. The shielding factor $B_{attenuated}/B_{applied}$ is referred to as the attenuation during this thesis, since this value decreases towards zero quite rapidly inside a superconducting cylinder it is usually interpreted logarithmically (in dB) and has SI unit Bell (20 dB = factor 100).

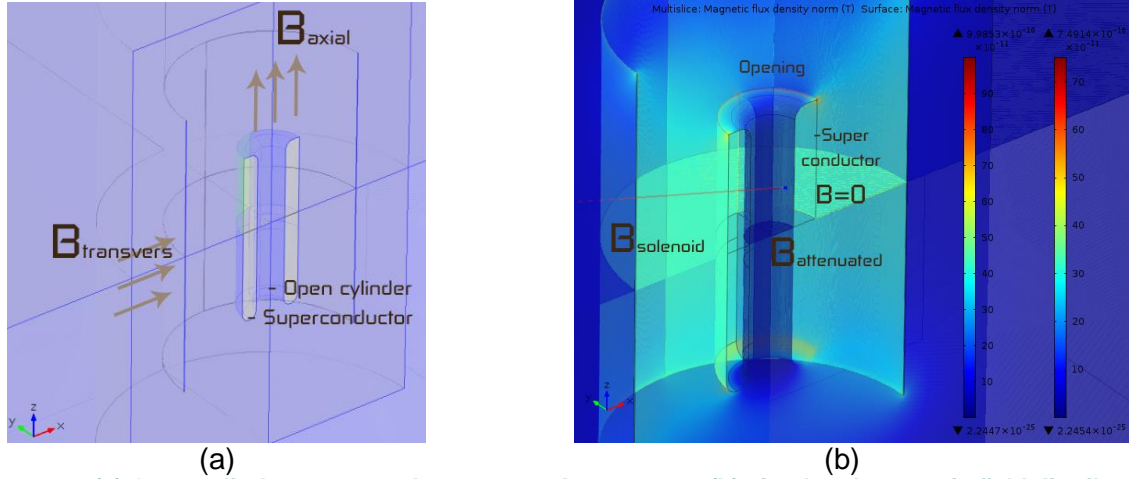


Figure 12. (a) Open cylinder superconductor example geometry, (b) simulated magnetic field distribution around superconducting open cylinder geometry.

$$A^{-1} = B_{attenuated}/B_{applied} \quad (12)$$

According to [x] the amplitude of B_{axial} inside a cylinder of superconducting material will decrease exponentially, with equation:

$$B_{attenuated} \cong B_{applied} e^{-3.83 z/a}, \quad (13)$$

where z is the depth in the cylinder and a is its radius.

A different attenuation function was found for a transversally applied magnetic field $B_{transversers}$, with an exponent factor differing from (13), given as:

$$B_{attenuated} \cong B_{applied} e^{-1.84 z/a}. \quad (14)$$

In the case of a non-axial (z -axis) symmetric magnetic field, an effective attenuation is expected as a sum of equations (13) and (14) for the axial and transversal components respectively:

$$A_{effective}^{-1} \cong n_{axial} e^{-3.83 z/a} + n_{transversers} e^{-1.84 z/a}, \quad (15)$$

where:

n_{axial} , $n_{transversers}$ are the normalized ($n_{axial} + n_{transversers} = 1$) components of the magnetic field in axial (z -) and transversal (xy -) direction. The for equation (15) the pre-factor is geometry dependent, which can be determined through modelling or measuring.

This resembles the Eigen-mode expansion technique applied for only the 2 most dominant modes from the axial and radial (or transversal) cross-sections of magnetic field propagation inside a superconducting cylinder.

3.5 Finite element model for magnetic attenuation

A theoretical explanation for the Meissner effect is found by combining London's equation (with penetration depth λ) and Maxwell's formulation of Ampère's law. London's equation is given [iv] as equation (16):

$$\nabla \times J = -\frac{1}{\mu_0 \lambda^2} B. \quad (16)$$

Modelling of magnetic fields from persistently flowing currents is done by solving differential equation:

$$\nabla \times B = \mu_0 (J + \epsilon_r \epsilon_0 \frac{\partial E}{\partial t}), \quad (17)$$

known as Maxwell's differential equation for Ampère's law where:

B is the magnetic flux density, (T)
 J is the current density I/Area, (A/m²)
 $\frac{\partial E}{\partial t}$ the electric field partial derivative to time. (V/m/s)

After substitution of J in equation (17) by the function of λ and B from equation (16) one finds:

$$\nabla^2 B = \frac{B}{\lambda^2}, \quad (18)$$

which is valid in a static (time constant with $\frac{\partial E}{\partial t} \rightarrow 0$) case. This is similar to Maxwell's equation (Gauss's law), $\nabla^2 B = 0$. Gauss's law only equals (18) for the limit $\lambda \rightarrow \infty$ (non superconductor).

The component perpendicular to the superconductor surface is set as, $B_{\perp} = 0$ by replacing the surface outside of the superconductor by a Neumann boundary condition with a vanishing normal component. No flux is allowed to go in or out of this boundary in the simulation. For all other areas Gauss's law for magnetism must be satisfied, all flux entering a closed area also exits this area, this way the field distribution in a finite area can be solved.

Using the AC/DC module in COMSOL Multi-physics the attenuation of an arbitrary solid shape of superconducting material can be modelled by excluding its shape from the volume for the magnetic field to be solved in.

This works well for macroscopic superconducting objects such as wires and cylinders, or arbitrary geometries several times thicker than λ (London penetration depth).

For the magnetic shield engineering models these models have been presented [xi] at the 2013 COMSOL conference and are analysed (Ch. 5.1.1) for the relevant experiments described in this thesis.

Previous work in the *magnetic shielding* project show an agreement between the measured and modelled attenuation profile for an open cylinder shaped superconductor, a radial 2D profile of this model (plotted with uniform field line density and colour coded flux density B) is given in Figure 13.

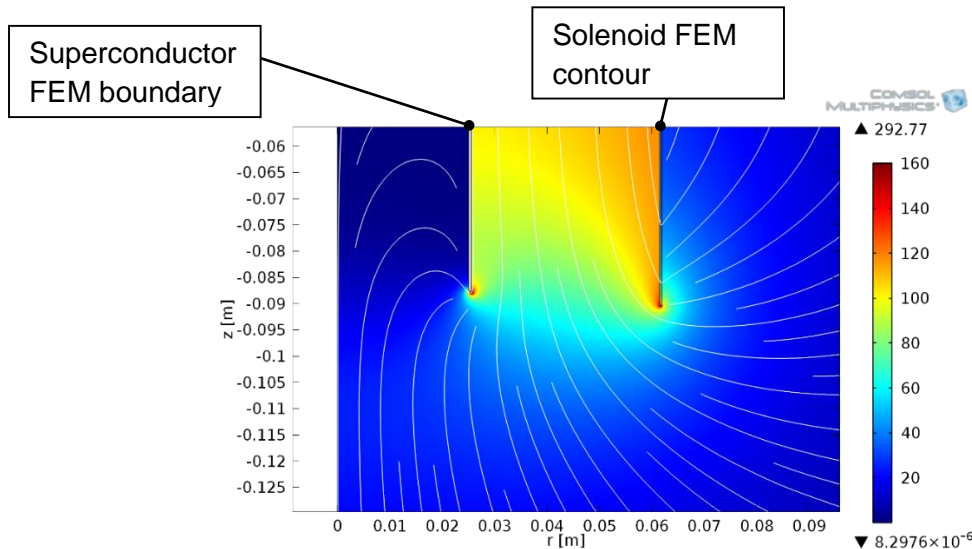


Figure 13. 2D FEM flux density result (color coded) of superconducting boundary inside a current carrying finite solenoid.

As can be seen in Figure 13 the magnetic field lines cannot pass through the boundary of the superconducting cylinder on the left, they can pass through the solenoid coil material on the right. These computational models are known to be accurate for superconductors in the Meissner state, superconductors mixed Meissner (vortex) state behave differently from this model above the lower critical field or around the critical temperature ($T_c = 9.22$ K for niobium).

3.6 Magnetometer theory

This paragraph will explain the theoretical differences between the used magnetometers. A dc-SQUID magnetometer was used for measuring the attenuation, cryogenic fluxgate magnetometers were used for calibration and phase transition measurements.

3.6.1 dc-SQUID magnetometer

The basis of a Superconducting Quantum Interference Device as a magnetometer is the magnetic field expulsive property of superconductors. The ring of superconducting material (see Figure 14 (a)) can freeze in a constant magnetic field when it goes through the phase-transition. Any change in this flux ϕ_B will cause an extra current in this ring that cancels this flux.

The dc-SQUID is a loop of superconducting material with 2 Josephson Gates (Tunnel Junctions) where electrons will have to tunnel through to sustain a current across the connection, see Figure 14 (b).

In case the induced magnetic flux changes, a current will start running to compensate this in periods of the flux quanta ϕ_0 . By counting the amount of peaks that pass by on the signal and knowing the area A of the SQUID, the magnetic flux measured can be calculated as $B = n\phi_0/A$.

Now the field cancelling current will oscillate as a function of the externally applied magnetic field, with a period of the flux quanta ϕ_0 . See reference [xii].

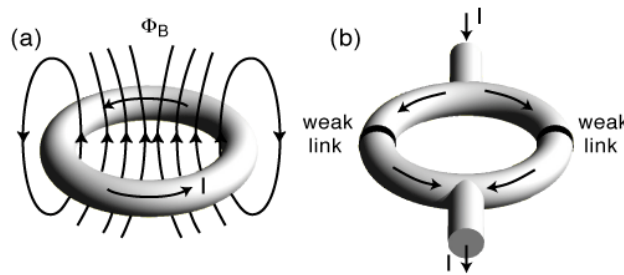


Figure 14. (a) Illustration of (a) superconducting ring, (b) dc-SQUID or ring with 2 Josephson junctions. Source: (<http://users-phys.au.dk/philip/pictures/physicsfigures/>).

To measure the absolute magnetic field with this oscillating output signal would require the operator to count how many periods go by when the dc-SQUID is rotated through the maximum and minimum of the external magnetic field, which has been done with counting rates around 2000/sec according to [xv]. A more linear way of measuring can be achieved by using a negative feedback system illustrated in Figure 15, which locks the signal of the dc-SQUID to a constant value on the slope of the sinusoid. With this method the feedback coil used to counter the externally applied flux will have a current running through it which linearly changes with the change in flux following equation (19).

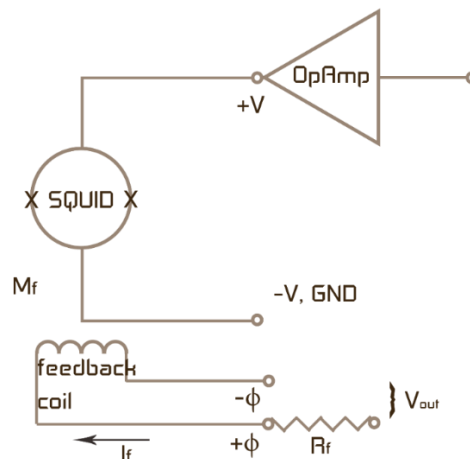


Figure 15. Simplified electronic circuit for feedback coil of a dc-SQUID.

For the voltage read out when the SQUID is in flux locked loop mode, the measured magnetic flux density is given by equation (19):

$$B_{SQUID} = \frac{S_{\phi} \cdot M_f \cdot I_f}{R_f}. \quad (19)$$

When measuring a magnetic field B with a SQUID, the resulting read out FLL – voltage follows a sine function with a period of ϕ_0 . This is the flux quanta of $\phi_0 = \frac{h}{2e} = 2.07 \cdot 10^{-15} \text{ Wb}$ or $B_0 = \phi_0/A$ (T) with A being the perpendicular area in m^2 of the flux loop to the magnetic field lines. The phase in a superconducting loop is quantised by $2\pi n$, where n is the an integer amount times the minimal flux quanta ϕ_0 . See reference [xv].

See reference [xiii] (Chapter 7) for further reading on SQUID theory.

3.6.2 Fluxgate magnetometer (cryogenic)

The principles of the fluxgate magnetometer have much less to do with quantum mechanics theory than the SQUID magnetometer. The advantage of a cryogenic fluxgate detector is that versions are available which will operate for every temperature between +30° C (room temperature) and 4° K (liquid He), allowing measurements to be repeated outside of the Dewar or during cool down.

A wire wound around a high permeability metal is used to shake the magnetization of the metal core, the response in a 0 field is known and the response in a constant field in the sensitive direction of the wound coil is calibrated. The hysteresis of the ferromagnetic material in the core is exploited, as the excitation coil rapidly magnetizes the core into saturation, the readout coil will detect the signal of the change in flux which will in turn be a measure of the absolute flux in the sensitive direction. See [xiv] for more detailed theory about ferromagnetism.

The electronic control box (in the Bartington setup) can derive this DC component of the flux in the fluxgate to ~2 nT accurate.

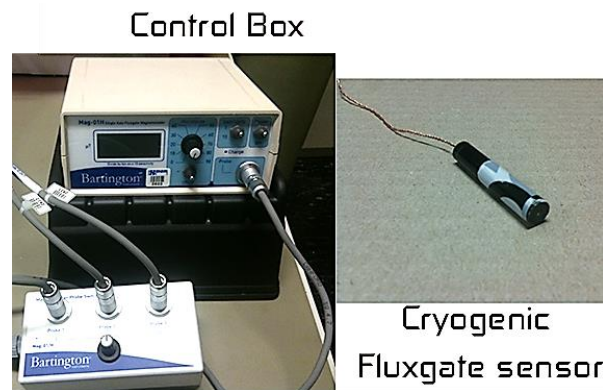


Figure 16. Images of used cryogenic fluxgate (Bartington) setup, Mag-01H readout box with 3 type F probes.

3.6.1 Measuring flux density vector \vec{B}

To compare the measurements from the two types of magnetometers, it can be useful to split the magnitude and direction of the field into different components. A rotatable SQUID will can be used to measure 2 spherical components (rotated 180° to solve a possible locking offset), whilst a fluxgate can measure the absolute component in a certain direction (z-component has been measured).

When one measures the vector of the magnetic field density \vec{B} , there are 3 Cartesian coordinate components, namely B_x, B_y, B_z , that define the magnitude B and direction \vec{n} .

$$B = \sqrt{B_x^2 + B_y^2 + B_z^2} \quad (20)$$

With direction given as unit vector \vec{n} .

$$\vec{n} = \begin{pmatrix} B_x/B \\ B_y/B \\ B_z/B \end{pmatrix} \quad (21)$$

The used magnetometers are direction sensitive and will measure only the component of B in the sensitive direction $B_{measured} = \vec{B} \cdot \vec{n}_{measured}$.

When rotating such a detector direction in 2 of the spherical coordinates the vector \vec{B} can also be derived from the measured component maxima and corresponding angles θ_{plane} as:

$$\vec{B} = \begin{pmatrix} B_{xz} \cos(\theta_{xz}) \\ B_{yz} \cos(\theta_{yz}) \\ B_{xz} \sin(\theta_{xz}) \vee B_{yz} \sin(\theta_{yz}) \end{pmatrix}. \quad (22)$$

To accurately calculate the magnitude $|B|$ with direction \vec{n} , a minimal error in both angle and signal should be made.

With a 3-axis fluxgate magnetometer, where each fluxgate is pointed along a different axial direction, the magnitude and direction can be retrieved without rotating, using equation (20).

3.6.2 Error analysis

The inaccuracy in measurements from the specifications of the magnetometers are presented in Table 1.

Table 1. Literature magnetometer errors from manufacturer specifications.

Magnetometer type	ΔB (magnitude error in nT)	$\Delta\theta$ (pointing error in °)
Bartington fluxgate	2 (3 nT from absolute 0)	.3
PTB SQUID	.02 (for 7 nT/ ϕ_0)	.3 (see 8.4)

An error propagation to the final calculated magnitude and direction is expected. For 3-axis fluxgate measurements the final error adds up according to equation (23):

$$\Delta|B| = (\Delta B_x + \Delta B_y + \Delta B_z) + B_x \sin(\Delta\theta_x) + B_y \sin(\Delta\theta_y) + B_z \sin(\Delta\theta_z), \quad (23)$$

with inaccuracies in measurement of $\Delta B, \Delta\theta$ from magnitude and pointing direction respectively (note that $B(\theta) = |B|\cos(\theta)$ is used for this derivation). From the given literature inaccuracies this error would be approximately $\Delta|B| \sim (6 \text{ nT} + 1\%|B|)$.

The angular error for the SQUID dipstick was investigated in measurement report 8.4 in the appendix. This showed a hysteresis present in the setup of $\sim 5 \pm 5^\circ$.

4 Experiments

In this chapter the measurement and experiments discussed in the strategy (Ch. 1.4.4) are described in detail. First the attenuation measurement, secondly the phase transition experiment.

4.1 Attenuation measuring setup

As a SQUID is the more sensitive magnetometer, this detector will be used to measure the 0.1~1 Hz AC signal left inside the shield sample (when superconductive). Magnicon hardware is used to control the SQUID via the computer. Also the current source in the Magnicon brick is used to power the solenoid inside the Insert.

An overview of the used parts and required connections between them are given in Figure 17.

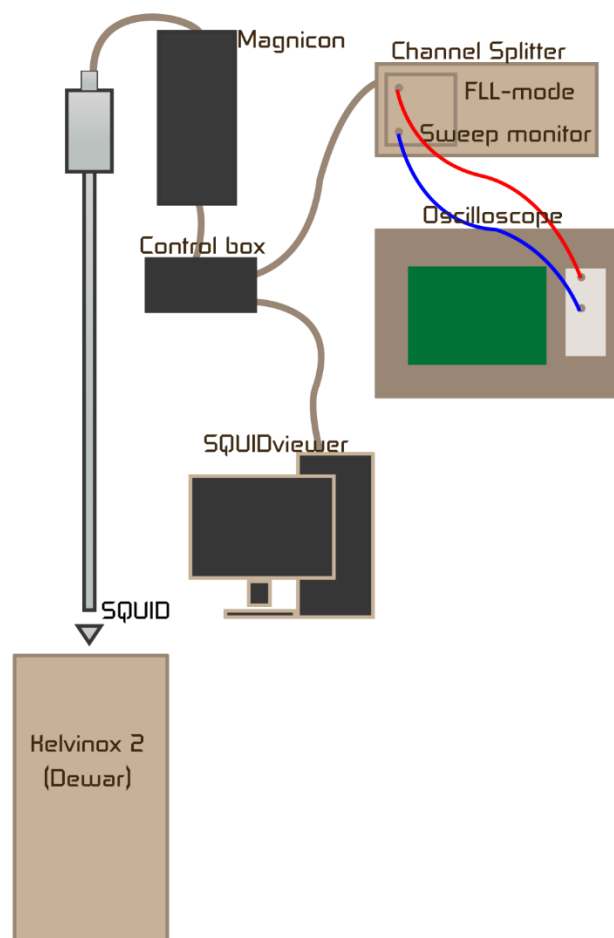


Figure 17. Illustration of the equipment (not to scale) used when measuring with a SQUID at 4.2K (liquid He temperature).

The oscilloscope was sometimes replaced by a data acquisition card (DAC), which in turn is connected to the PC by optic fibre cable.

4.1.1 Insert

To hold all the parts of this experiment in the correct place, an insert for the Kelvinox II cryostat is used. From where the setup is suspended on three ~1.5 m long wires from the valve.

During a cryogenic experiment a visual mark can be placed on the long tube of the dipstick at the point where the bottom of the dipstick touches the 0,0 mm reference plate in the Insert, this allows to measure the exact distance z_{ref} the dipstick is lifted and avoid large positioning errors due to length contraction differences.

The micro-meter on top of the dipstick is used to measure the SQUID's rotation angle θ_x around the x-axis.

With the laser mod on the casing of the dipstick rotation angle θ_z can be measured with an accuracy of $\pm 1^\circ$.

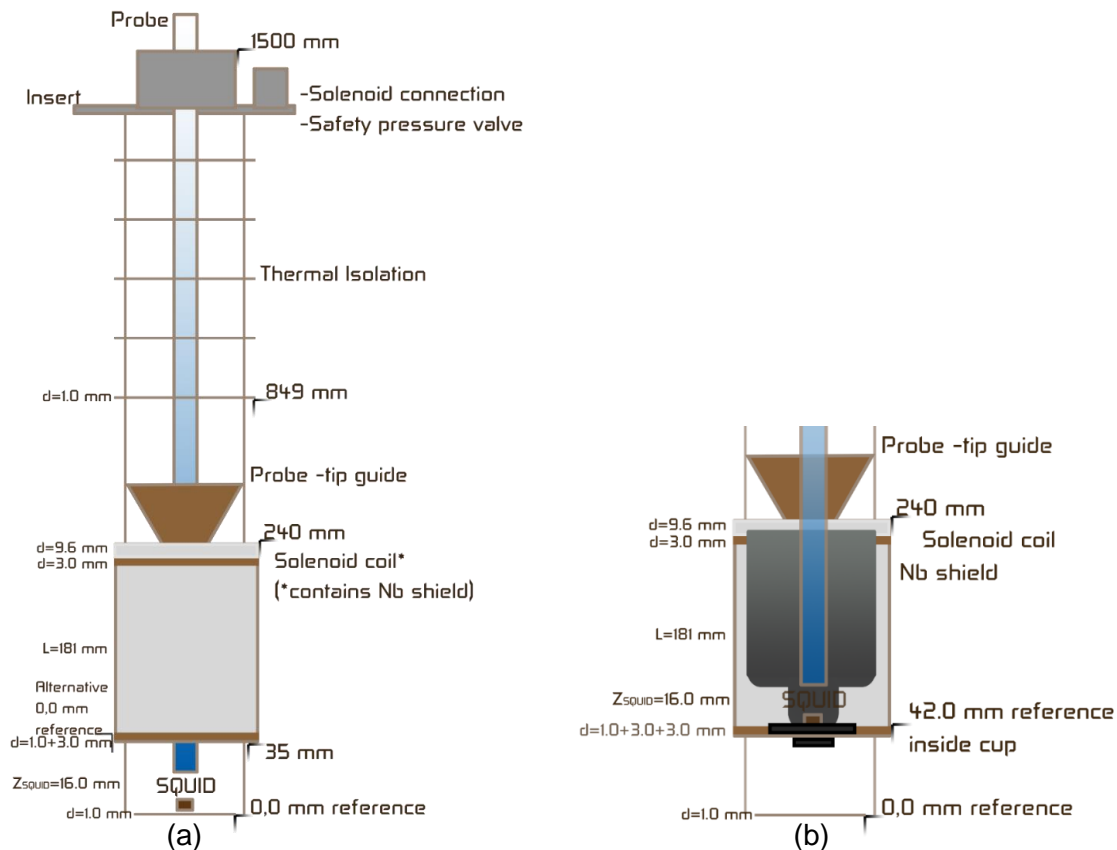


Figure 18. Illustration of the Insert with SQUID probe mounted inside, this is our reference frame for moving the SQUID probe (a) through the solenoid or (b) niobium magnetic shield.

In Figure 18 (a) is derived that the centre of the solenoid will be at a reference height of 113.5 mm, as the SQUID is positioned at $Z_{SQUID} = 16.0$ mm from the reference bottom plate and the solenoid centre is at $\frac{L}{2} + d + 35$ mm. L is the length of the solenoid coil, d the thickness of coil holder (3 mm) and aluminium plate (1 mm). *More detailed engineering designs of setups (a) and (b) from Figure 18 are given in Appendix A: Technical designs.

When the closed cup shaped Niobium shield is placed inside the solenoid, the probe will no longer be able to touch the reference 0.0 mm plate. This is illustrated in Figure 18 (b), where a minimum height for the probe of $42 \pm .5$ mm relative to the reference plate is reached.

4.1.2 Dipstick

The dipstick used for the attenuation measurements has a SQUID magnetometer mounted on a rotatable holder at the end of the stick (16 mm from the bottom), see Figure 19.



Figure 19. Image of dipstick part containing the '3D' SQUID.

By rotating the micro-meter on top of the dipstick the SQUID is rotated around the chip-holder axis. Which has an angular offset around the z-axis of $+7.5^\circ$ from the 0° reference x-axis.

In order to accurately read out the angle of rotation around the z-axis a modification is made* to the dipstick, a laser mounted on the dipstick and a degree scale fixed to the Insert provide a more accurate and repeatable θ_z angle read-out than previous methods. See Figure 20 for this modification.

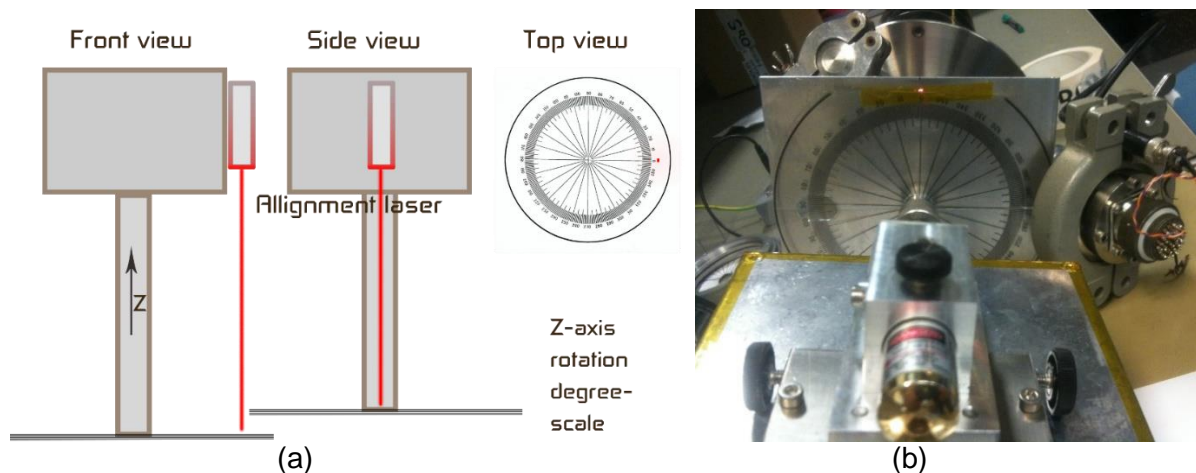


Figure 20. (a) Illustration of laser modification for readout of z-axis rotation angle of the dipstick. (b) Image of the aligned laser modification on the 3D SQUID dipstick in the Insert.

There was an offset measured in the xy-plane between the direction perpendicular to the connector box plate upon which the laser is mounted and the rotation axis of the SQUID of $\theta_{xy-offset} = 7.5^\circ$ rotated counterclockwise around the positive z axis. It was also noted that there is a variation in this angle possible of $\sim \pm 2^\circ$ by applying torque, from where it would return to the starting position by mechanical forces within 0.5° , this is a potential systematic measurement error if the dipstick is suspended using the crane above the kelvinox II cryostat.

4.1.3 XYZ Reference coordinate frame

Here the reference frame used in describing the measurements is defined. The measurements and calibrations done follow these definitions for the (x, y, z) axes:

- Z-axis points in the direction of the length of the dipstick,
- Y-axis points to $+90^\circ$ on the XY-plane from the X-axis,
- X-axis is the axis rotated about by turning the micro-meter,

where the XY-plane has the direction away from the wall, parallel to the windows defined as 0°. This is illustrated in Figure 21 where the layout of the cryogenics lab is given.

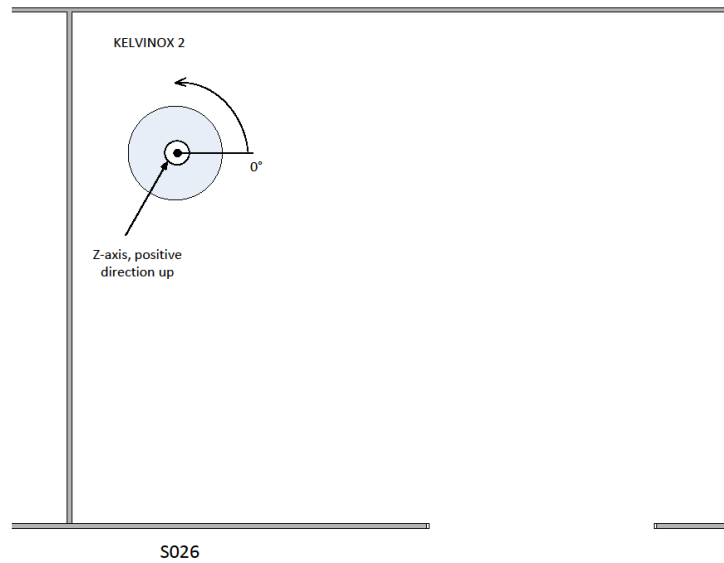


Figure 21. Kelvinox 2 its Z-axis reference in room S.026, the 0° line in direction parallel to the windowed wall. (original by Caspar Bruineman)

With a mark on the table of the Kelvinox 2 the goniometer illustrated in Figure 20 can be aligned to this reference.

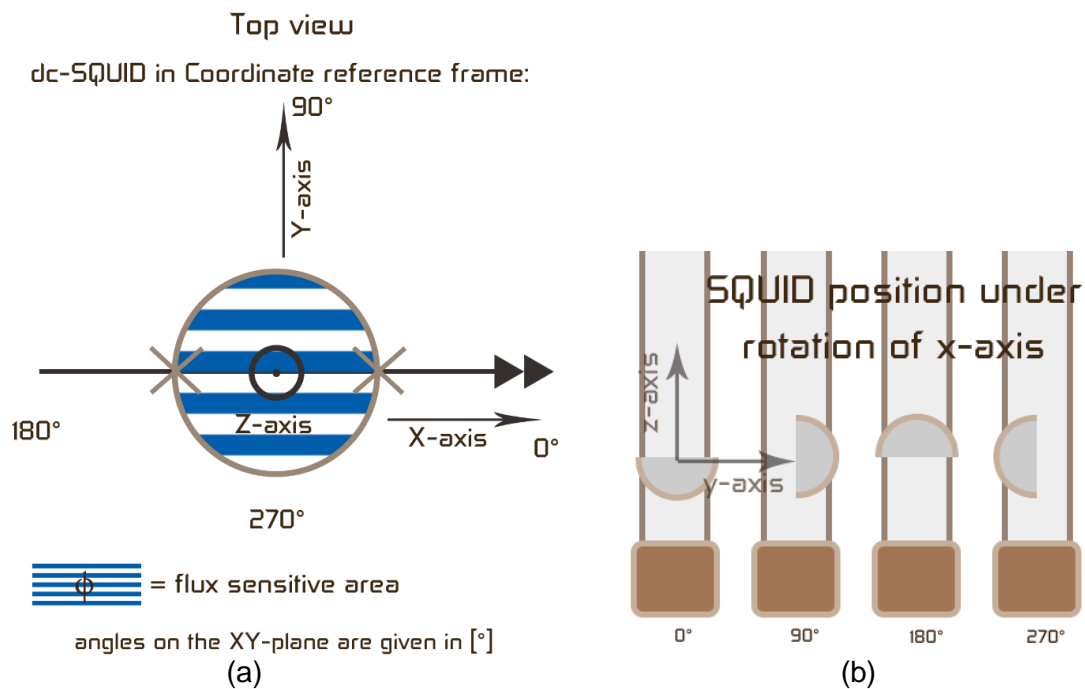


Figure 22. (a) Illustration of the reference coordinate system of the SQUID inside Kelvinox 2. (b) SQUID position inside probe tip at 4 x-rotated positions, the x-axis is defined with the right-hand rule relative to the zy-plane.

Flux ϕ in Figure 22 (a) is measured with the normal along the z-axis, but the SQUID can rotate around what in this configuration is the x-axis (when rotated 90° counterclockwise this would be the y-axis inside the Kelvinox 2 coordinate system). A rotation of the dipstick will always be around the z-axis. Therefore this setup meets the minimal requirement of 2 free

axis of rotation in order to measure flux from most of the possible 3-dimensional directions to the measuring tip.

A side view from $\theta_z = 0^\circ$ is given in Figure 22 (b) for different positions of the micrometer at specific rotation angles. For angles 90° and 270° the SQUID will not measure any component of a signal applied in the z-direction, while at 0° and 180° it will measure the maximum z-component.

Rotating the micro-meter from < 20 mm up to $21.0 \pm .1$ mm effectively points the SQUID in the direction of the z-axis. The SQUID will rotate with a transfer of $14.3^\circ/\text{mm}$ in the range $1 \text{ mm} \rightarrow 21 \text{ mm}$, above and below the transfer deviates from this value.

4.1.4 Solenoid Amplifier Circuit

To measure attenuation factors below 10^{-5} a higher current was required than the current source of the Magnicon 1 electronics could produce. Therefore a Power amplifier that has a flat frequency response for low frequent signals is used to generate a current of maximally 1 A. This had to be done while keeping the power dissipation in the solenoid to a minimum, to prevent breaking or melting the wiring. The circuit in Figure 23 was used to amplify the current output of the electronics setup by a factor of 10.

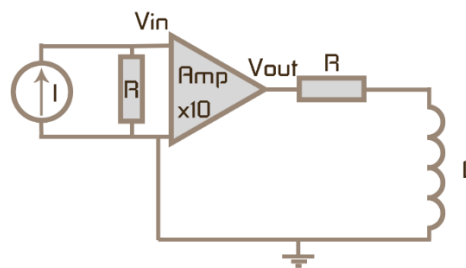


Figure 23. Current amplifier circuit for solenoid, with $R=330 \text{ Ohm}$.

The amplifier used was put on AC + DC mode, this way it is capable of amplifying the .1 Hz frequency range of the input voltage V_{in} .

4.1.5 Fluxgate calibration setup

Three cryogenic fluxgate magnetometers were calibrated on their sensor direction inside the casing. Also the 2-axis Helmholtz coil setup was characterized by a fluxgate aligned by a scanning rod.

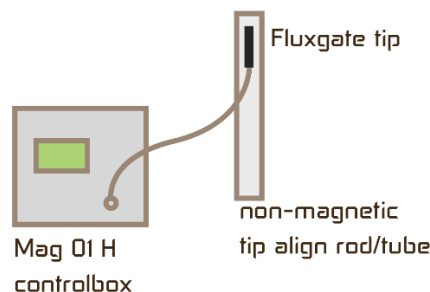


Figure 24. Illustration of fluxgate magnetometer setup.

The fluxgate magnetometer is connected to a control box to read out the calibrated measured flux in the sensitive direction of the measuring tip. The probe inside the tip casing is 30 mm long, the average measured position is in the centre of the probe.

4.2 Phase-transition trapping Experiment

For this experiment the shield sample is lowered into the liquid He inside the cryostat under various magnetic field exposures. The effect of trapping magnetic flux by uncontrolled (from multiple points) cooling is investigated. In follow up experiment (Ch. 4.3) a cooling method to prevent this trapping of flux is used.

4.2.1 Setup

Again the cryostat and insert are used, but with 2 fluxgate sensors mounted at the bottom and top part of the shield sample. These fluxgates allow to measure the remnant field of the cryostat in the z-direction as long as the sample is normal. In Figure 25 the 2 positions chosen for the fluxgate detectors are illustrated.

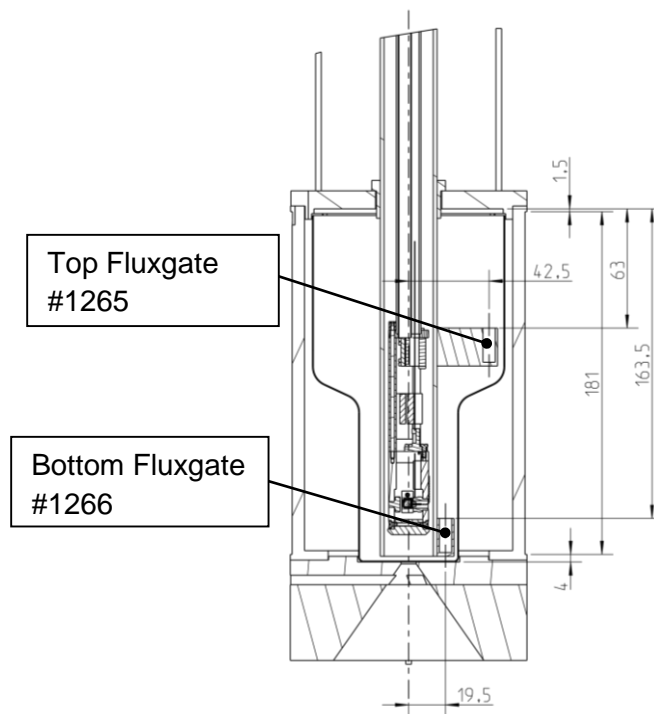


Figure 25. Phase-transition measurement setup with cryogenic fluxgate magnetometers.

With the Bartington control/ switch box the readout of the fluxgates could be switched between, only one can be operated at a time. The entire insert is lifted in and out of the cryostat for this experiment, instead of using a dipstick with a magnetometer at its end. The SQUID dipstick was not used during these measurements.

To cool down the shield sample, the entire Insert setup was gradually lowered into the cryostat. When the depth of the bottom of the setup approached the liquid He level small ~cm steps were made to gradually cool the sample from bottom to top. When fluxgate #1266 would become insensitive to changes in the external magnetic field, the bottom of the sample is assumed to be below T_c . The same is assumed for fluxgate #1265 and the top of the sample.

4.3 In-field cooling Experiment

As a proof of concept for the suggested ‘progression controlled cooling’ technique [ix], the shield sample is cooled down with a presumably larger temperature gradient. This should allow the expulsion of the magnetic field from the shield. As this Meissner phase front expands from the point of cooling to the top of the shield sample, all magnetic flux could be expelled from the shielded volume. If local flux pinning occurs at material impurities or lattice imperfections, these might end up trapped in the shield if not overcome by the temperature gradient.

4.3.1 Modified setup

A copper cooling rod was added to the fluxgate measurement setup. This should prevent the bottom of the shield from trapping magnetic flux, as it touches on a single centered point with the copper cooling rod.

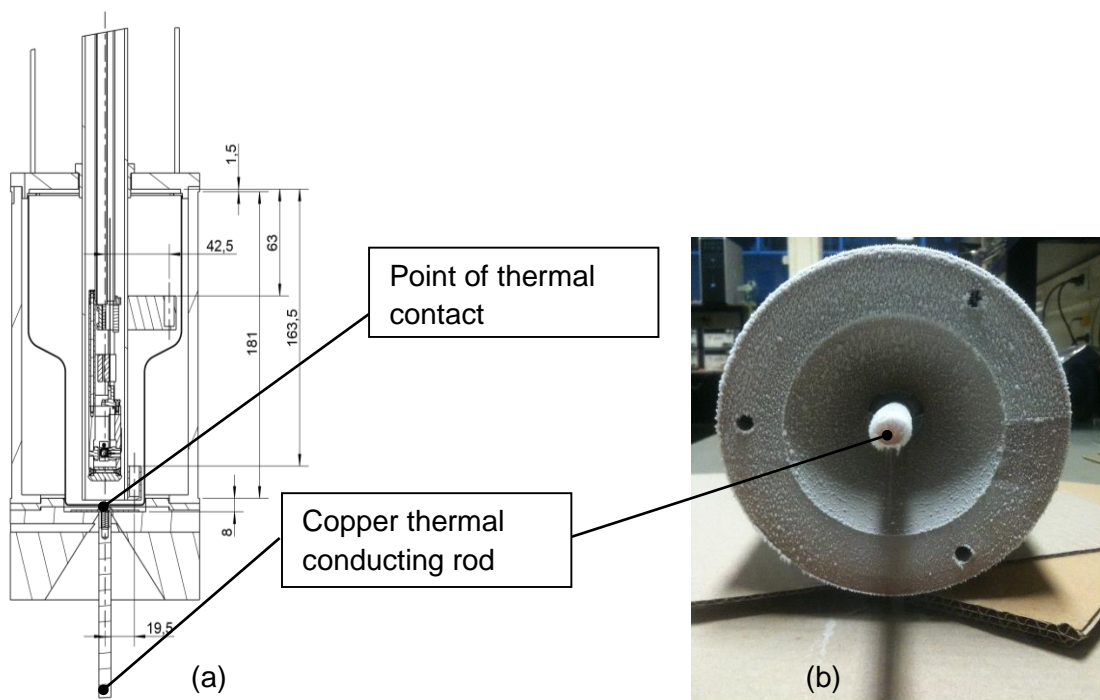


Figure 26. (a) Design cross-section, (b) image, of point cooling modified setup.

This setup is also lowered into the cryostat by sliding the entire insert down. The copper rod will first make contact with the liquid He and starts to cool first, ensuring a temperature gradient from the thermal contact to the top of the shield sample.

5 Summarized Results/ Additional Data Analysis

In this chapter the combined results from the measurement reports (found in Appendix B: Measurement reports) are discussed and further analysed.

Research question I (from Ch. 1.4.2) is answered by the new attenuation measurement of the closed Nb cup in Ch. 5.1. New attenuation measurements allowed the characterization of the attenuation nearer to the bottom of the shield. A better fitting is achieved with the (geometrically improved) COMSOL model for the attenuation above the shield opening (investigated in Ch. 5.1.1). The divergence in 2D model and measured points near the bottom of the closed shield was further investigated with 3D modelling (in Ch. 5.1.2).

For research question II (from Ch. 1.4.3) experiments were done, of which the initial results are consistent with previous measurements done on the closed Nb shield sample. Field cooled magnetic flux expulsion as suggested by [ix] was observed in the point cooled experiments (Ch. 5.5).

After a second modification (copper cooling rod) to the setup, allowing to cool from a smaller area on the bottom of sample, a different result was observed. Residual magnetic fields of the cryostat in the order of ~ 100 nT were successfully expelled from the bottom half of the shield sample. Flux densities in the order of $1 \mu\text{T}$ or higher were not expelled, but observed to be trapped for $\sim 100\%$.

5.1 Closed Nb shield attenuation

For the single body (closed cup shape) niobium shield an attenuation (fraction $B_{attenuated}/B_{applied}$) of the signal B_z at the height of the TES, close to the z-axis, has been found to be below the order of 10^{-5} for $0 \text{ mm} < z < 80 \text{ mm}$.

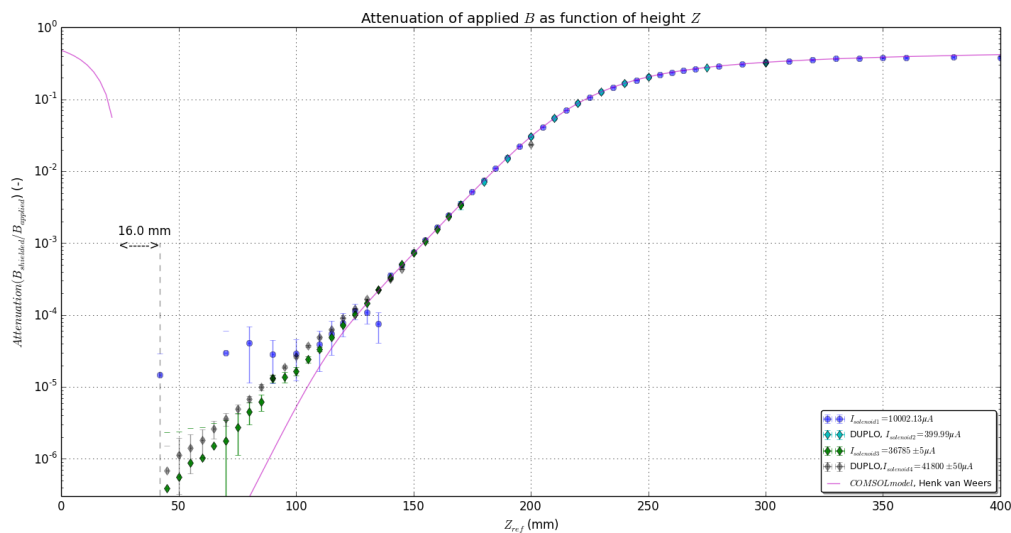


Figure 27. Measured attenuation of closed Nb shield compared with a 2D COMSOL model of the setup.

COMSOL model parameters were edited in order to correspond with ± 0.2 mm of the measured values, the geometry in a radially symmetric cross-section is seen in Figure 28.

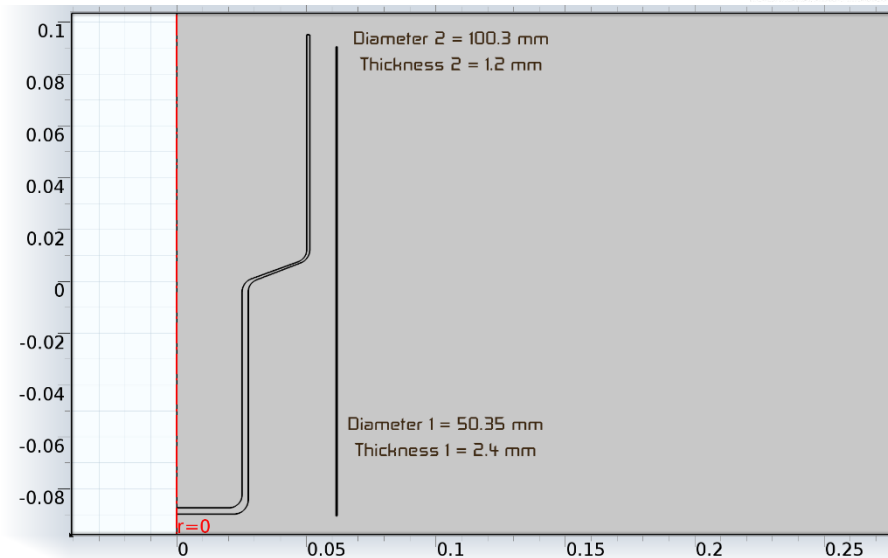


Figure 28. Modelled geometry as measured on the Nb shield by Hereaus, on date: 24 January 2013.

5.1.1 2D COMSOL model analysis

The perceived attenuation limit of $z > 300$ mm was strongly related to the radius ratio between the solenoid and the shield cylinder, for a smaller radius the model predicts a higher upper limit and a steeper attenuation slope for $z < 200$ mm. Also the height of the shield relative to the solenoid changes the resulting measured flux profile significantly. This flux confinement effect on the upper attenuation limit has been investigated by modelling various radii in COMSOL and is presented in Figure 29. This effect demonstrates the attenuation of nearby current loops surrounding a closed body Niobium shield.

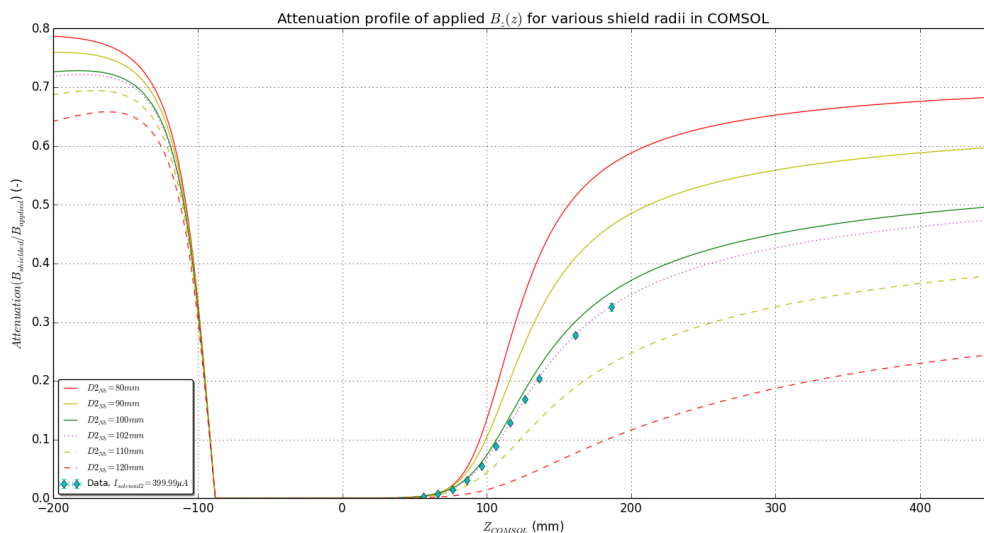


Figure 29 COMSOL modeling profiles for flux confinement effect on B_z attenuation profile.

From the COMSOL model the radially symmetric magnetic field generated by the solenoid are visualized in Figure 30 (a), the color indicates the flux density where the white lines are the ‘uniform density’ field lines. Note that in reality the field lines do not have a start and end point, but rather form closed loops, the polarity is also not indicated with arrows as the flux density profile is valid in both cases.

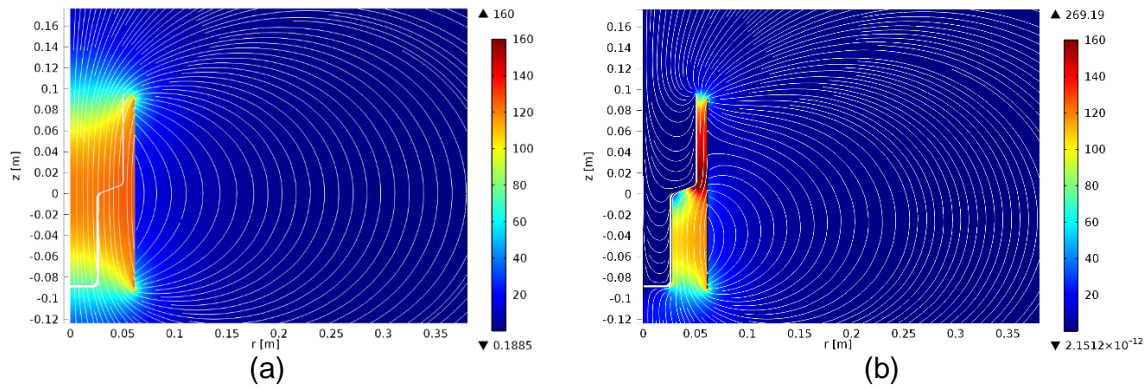


Figure 30. (a) COMSOL Model fitting measured solenoid profile, flux density B plotted as color. (b) COMSOL Model fitting attenuated signal profile, flux density in z -direction plotted as color.

To model the measured attenuated signal a thin superconducting area is marked where no magnetic field lines are allowed to go through, instead it can be seen in Figure 30 (b) that these bend back around the boundary when getting close. Field lines are allowed to pass through the solenoid coil as this is a conventional conducting material.

The COMSOL model used for this analysis, where geometrical parameters were edited to match the experiment setup, has been created at an earlier stage of the project.

*diameters in the plots above are 123 mm, 100 mm, 50 mm for the solenoid, D2_Nb, D1_Nb respectively. Lengths are 181 mm, 182.5 mm for solenoid, closed shield respectively.

5.1.2 3D Model analysis

To investigate the effect on the attenuation curve of an angular offset between the z -axis of the solenoid and the closed Nb shield, a 3D model was constructed (Henk van Weers). Here the expected decrease of attenuation by a transvers component of the magnetic field for various angle offsets can be analysed. See (15, where only a small fraction of the second exponent will become the dominant measured signal at otherwise highly attenuated positions along the z -axis. In Figure 31 (a) a cross-section of the magnetic flux density is given, Figure 31 (b) shows the field lines (for several points across the shield centre) that indicate the direction of the magnetic field at each point. Note that this simulation is no longer exactly radially symmetric, as an offset of 0.5° was given to the solenoid coil relative to the Nb shield to simulate a realistic and possible misalignment.

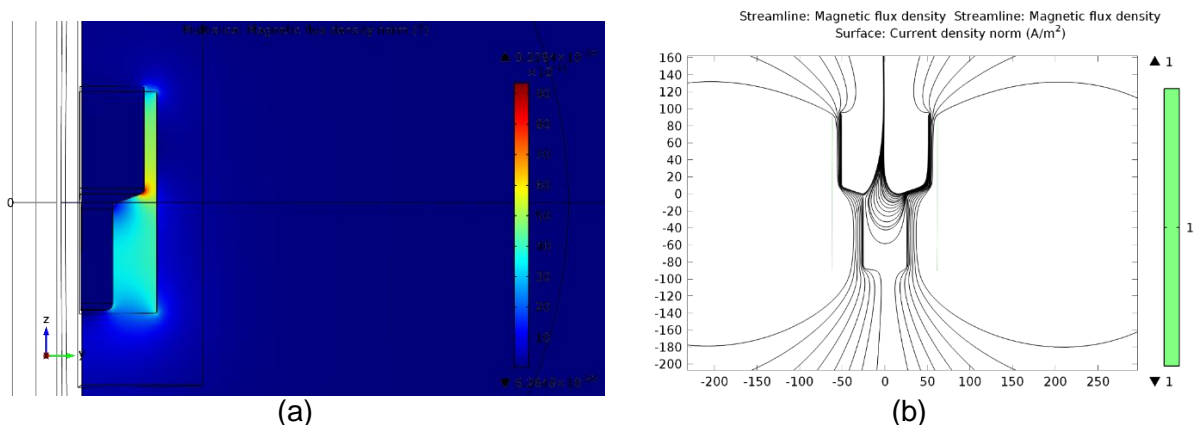


Figure 31. (a) Magnetic flux density in 2D plane of 3D Nb Shield model in COMSOL. (b) Magnetic field line profile by solenoid with 0.5° offset in z -axis, for radially equidistant field lines at $z=0$ (± 10 mm).

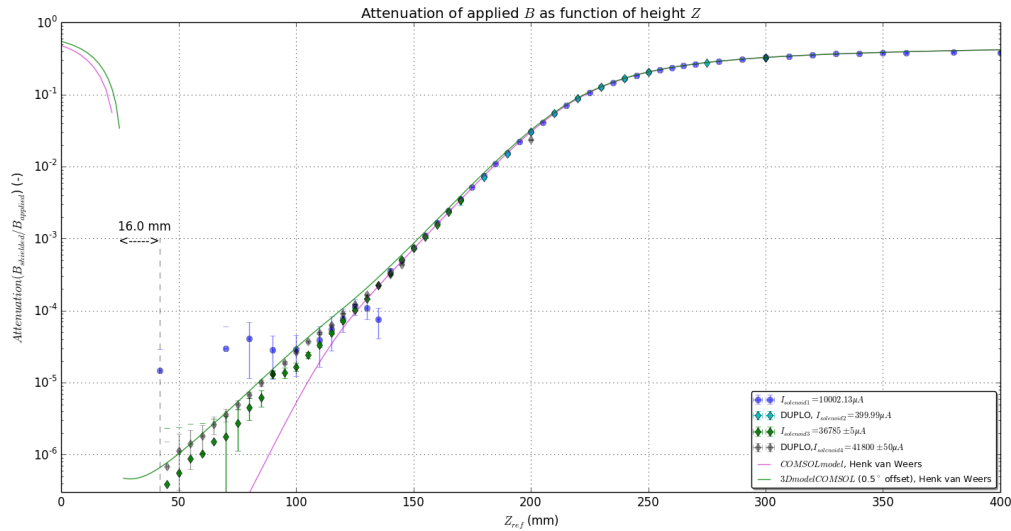


Figure 32. 3D model of $|B|$ fits for attenuation in B_z of closed Nb shield at an axis offset of 0.5° .

With the 3D modelled attenuation for a realistic axis offset the limit in attenuation of $\sim 10^{-6}$ can be partly explained, see Figure 32 for the comparison to the 2D case and measured data points. The exact angle of misalignment cannot be deduced from this fitting, as the pointing of the SQUID was not defined with enough precision (within $\sim 2^\circ$ of z-axis direction). It must be noted that there is a difference in plotted units for the 3D and 2D models, as magnitude $|B|$ does not necessarily point in the z-direction.

5.2 Opened Nb shield attenuation

The shield sample will, *after the writing of this thesis, have its bottom enclosure removed, as the small diameter tube will be then similar to the optical entrance in the final 2-part Niobium shield design.

With the extra non superconducting opening the signal from the solenoid is not expected to be as attenuated at the bottom. Both cases with identical geometry are presented in Figure 33, the data originates from the modified COMSOL model (see Figure 34). If no bottom shield would be added, there is only a small ~ 10 mm distance in z-direction where the attenuation would be sufficient.

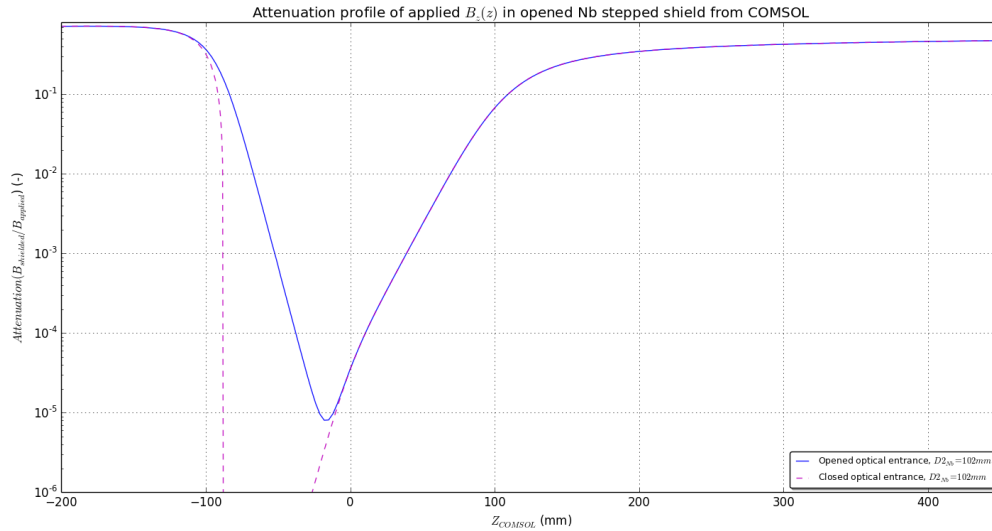


Figure 33. Open optical entrance vs closed attenuation profile of flux density on z-axis, simulation results.

Due to the inconsistency of the measured data and 2D model in the area of $A^{-1} = \sim 10^{-5}$, it is expected to measure a factor ~ 6 higher attenuation here.

In Figure 34 the magnetic flux density in a radial symmetric plane is given. The lowest flux density reached is a factor $\sim 10^{-5}$ of the solenoid generated flux density at that point.

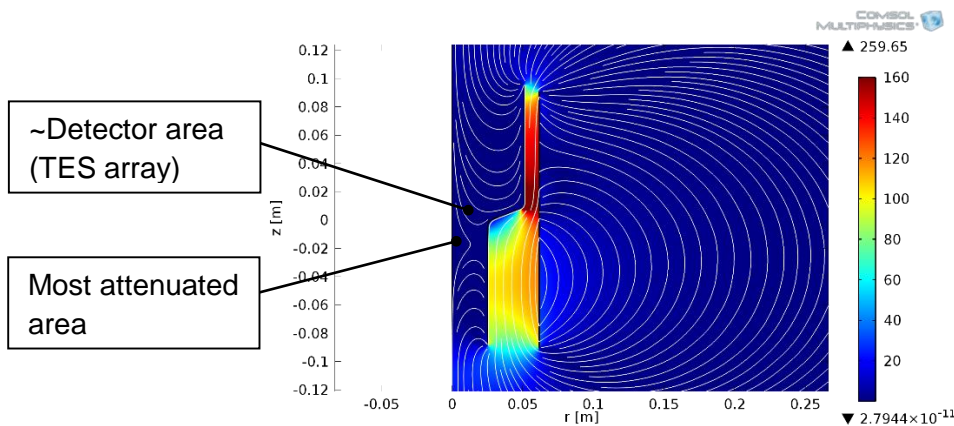


Figure 34. 2D radial symmetric COMSOL model of opened optical entrance, with $D2_Nb=102mm$.

5.3 *2-part Nb shield attenuation

*Not yet measured, as the 2-part shielding sample (from Hereaus) was not available at SRON at the time of writing this thesis.

5.4 *Cryoperm shield attenuation

The characterization of the two-axis Helmholtz coil setup was done (see 8.1), by measuring the magnetic field with fluxgate sensors along the axis of both Helmholtz coils (see report: Helmholtz x and y axis B profile). *This was not yet repeated with the Cryoperm shield in the setup, which allows the calculation of the attenuation.

5.5 Superconduction-phase transition

Several measurements (see 8.11 and 8.12) show that for a single body Nb shield (without holes) flux trapping occurs. Approximately 100% of the applied field was trapped repeatedly under different magnetic field configurations.

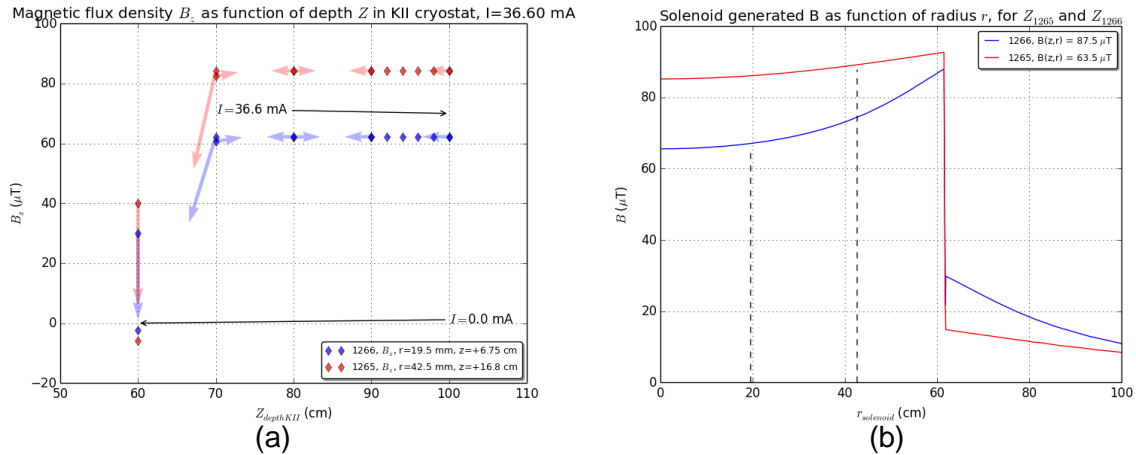


Figure 35. (a) Different flux density trapped measured per fluxgate, due to solenoid radial B profile. (b) COMSOL model data for magnitude B as a function of distance r from z -axis.

In Figure 35 (a) a plot of the highest trapped field (negligible KII remnant field) is given, during cooling through T_c a current of $I = 36.6$ mA was applied. The current $I = 0.0$ mA whilst raising of the shield sample to a height above the liquid He, but no change in magnetic field was measured until $Z = 70$ cm. When $T > T_c$ at $Z < 70$ cm the trapped flux is released and the lower (opposite polarity) remnant field at this height in the cryostat is measured again.

Nulling the magnetic field with an external coil just before cooling through T_c effectively trapped a close to 'zero' (25 ± 25 nT) remnant field in z -direction (see measurement report in 8.12 in appendix). This is possible for the measured B_z at both fluxgate positions.

Point cooling experiment:

When cooling the closed shield from a single point on the surface with a high enough temperature gradient, some expulsion of the magnetic field from inside the shield was suggested to be possible. This was observed to happen only in the bottom of the shield (with fluxgate #1266), using the modified point cooling setup (with copper rod).

A plot of the observed flux expulsion is given in Figure 36. When repeating the cooling process without heating (lifting higher in the cryostat) first caused a flux density higher than 0 ± 3 nT to be trapped. This is assumed to be due to the decreased temperature gradient. Also applying an external magnetic field with the solenoid, after the expulsion, introduced a trapped flux in the already cooled shield. For a $64.0 \mu\text{T}$ applied (after cooling to below T_c), a $.2 \pm .1 \mu\text{T}$ flux density was measured to become trapped at the bottom fluxgate position.

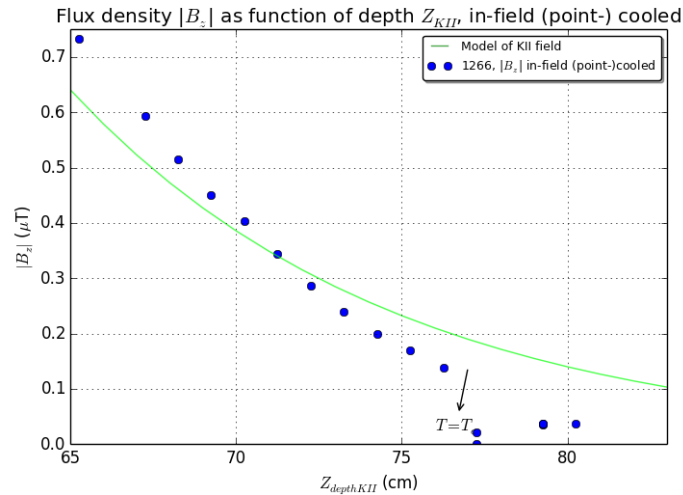


Figure 36. Magnetic field z-magnitude as a function of depth in cryostat, note the sudden drop to 0.0 at 77 cm.

Previous measurements in this cryostat indicated a reversal in magnetic field direction along the depth in the cryostat, the first depth where this occurred was at ~100 cm for the Kelvinox II. The measurement of expulsion in Figure 36 occurred at a position with a remnant cryostat field of $B_z > 100$ nT.

Macroscopic material imperfections, presumably due to the fabrication process, of the shield sample were observed, see Figure 37 for the curved edge with ‘cracks’ on the surface.

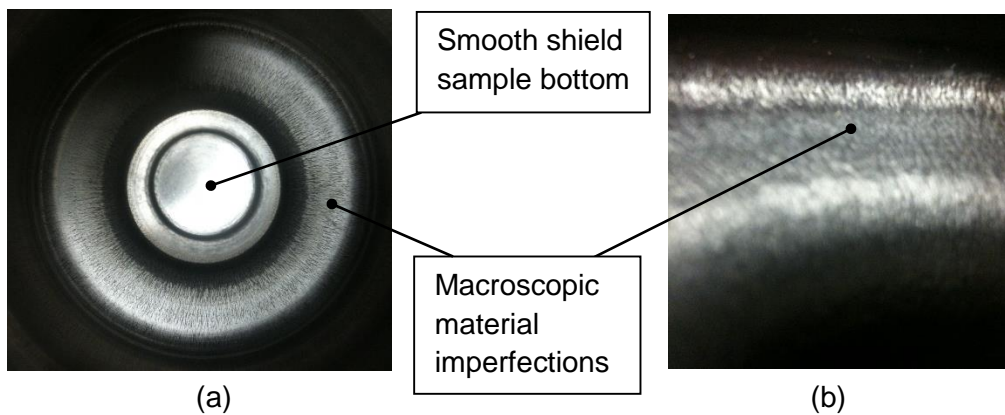


Figure 37. Images (a) top, (b) side view, of inside the shield sample (Hereaus), where a macroscopic crystal structure quality difference is observed between straight and curved niobium wall parts.

These local imperfections give an hypothetical explanation for not observing a flux expulsion from the top of the shield sample. At these cracks in the material the superconducting electron density n is expected to approach 0 m^{-3} for faults $\gg \lambda$. Here flux vortices would get ‘pinned’ as the Meissner effect will not be observed without enough superconducting electrons. When the top of the shield sample is cooled, the remnant magnetic field could now be topologically trapped through these pinning sites. Other theoretical scenarios are viable.

The effect that the trapping of magnetic fields in the shield has on its AC attenuation was not yet investigated. For applied field magnitudes far below B_{c1} no significant change is expected in the attenuation.

6 Conclusion

Measurements of the magnetic attenuation have been refined. Now the attenuation results are in closer agreement with the model of the measurement setup. The first discrepancy (different attenuation limit above the shield sample) was found to be an inaccuracy in the model, this limit was strongly top diameter dependent. The second discrepancy (difference in attenuation slope at the bottom of the shield sample) was attempted to be explained by a 3D model with an angular offset in shield from z-axis, but this result is not yet conclusive.

The requirement of the attenuation of B_z in the z-direction by the niobium shield to be below the order of $A^{-1} = 10^{-5}$ in the area of the detector is reached by this sample. At the bottom (of this 'closed' shield sample) an attenuation was measured of $A^{-1} = \sim 10^{-6}$, which from modelling is not expected to be reached for the 'opened' shield.

A 'zero field' cooled measurement (with 3D SQUID setup) showed a trapped flux of $\sim 2 \cdot 10^{-7}$ T, presumably the remnant of earth's magnetic field attenuated by the μ -metal cryostat shield. Actively nulling this residual in the z-direction was possible, where $\sim 2 \cdot 10^{-8}$ T was measured to be left (with the cryogenic fluxgate setup).

Follow up measurements with 2 fluxgate magnetometers allowed the characterization of the remnant field B_z in z-direction in the cryostat. Where for a liquid He cooled shield the magnetic field present during cooling was trapped ($\sim 100\%$). A modification to cool the Nb shield with He from a relative smaller area from the bottom resulted in comparable results.

When cooling the shield sample from a single point of contact with a cooling rod, a different result was observed from previous in field cooled measurements. A remnant field in the order of 100 nT could repeatedly be expelled from the bottom part of the sample, for 60~100% of the initial magnetic field magnitude. This efficiency decreases for higher magnetic flux densities (in this measurement setup), to effectively $\sim 0\%$ at 10 μ T.

References

- ^{ix} T. Golüke. "The influence of remanence and flux trapping on the magnetic shielding properties of mu-metals and superconductors." n.d.
- ^{xi} H.J. van Weers, C. Bruineman, G. Muckus. "Cryogenic Magnetic Shield Modeling & Verification." n.d.
- ⁱⁱⁱ R.A. Hijmering, P. Khosropanah, M. Ridder, J.R. Gao, M. Lindeman, H. Hoevers, J. van der Kuur, L. Gottardi, B. Jackson, R. Huiting, M. van Litsenburg. "Effect of Magnetic fields on Highly Sensitive TiAu TES Bolometers." (2010). Paper.

Above only the essential references to previous work are given, see the footnote for full the list of referenced works, literature and internet addresses.

Below a copy of the footnote from the end of this document is given.

-
- i. Official SRON website: <http://www.sron.nl/mission-and-strategy-about-sron-595.html>
- ii. Official JAXA website: http://www.ir.isas.jaxa.jp/SPICA/SPICA_HP/mission-en.html
- iii. R.A. Hijmering, P. Khosropanah, M. Ridder, J.R. Gao, M. Lindeman, H. Hoevers, J. van der Kuur, L. Gottardi, B. Jackson, R. Huiting, M. van Litsenburg, 'Effects of Magnetic Fields on Highly Sensitive TiAu TES Bolometers', (<http://resolver.tudelft.nl/uuid:516c9963-4a87-4469-ae4d-5da5e2132f2e>)
- iv. C. Kittel, (2004), *Introduction to Solid State Physics*. John Wiley & Sons. pp. 273–278. (ISBN 978-0-471-41526-8)
- v. C. Benvenuti et al, 'MAGNETIC FLUX TRAPPING IN SUPERCONDUCTING NIOBIUM', from CERN 1997 Workshop on RF Superconductivity.
- vi. J.D. McCambridge, 'The Superconducting Properties of Niobium-Titanium Alloy Multilayers', (<http://www.yale.edu/proberlab/Papers/McCambridgeDissertation.pdf>).
- vii. H.R. Kercher, 'Critical fields H_c and H_{c2} of superconducting niobium', (http://prb.aps.org/pdf/PRB/v24/i3/p1200_1).
- viii. P.E. Goa, 'Real-time magneto-optical imaging of vortices in superconducting NbSe₂', (<http://www.mn.uio.no/fysikk/english/research/groups/amks/superconductivity/files/sv.pdf>).
- ix. T. Golüke, 'The influence of remanence and flux trapping on the magnetic shielding properties of mu-metals and superconductors' (<http://essay.utwente.nl/63720/>).
- x. N. S. Alzayed, 'Magnetic Attenuation by HTC Superconducting Cylinders'
- xi. H.J. van Weers, C. Bruineman, G. Muckus, 'Cryogenic Magnetic Shield Modeling & Verification'.
- xii. R. L. Peterson, 'Sinusoidal Response of dc SQUIDs For rf Power Measurements'
- xiii. O.V. Lounasma, 'Experimental Principles and Methods Below 1K', ISBN: 0-12-455950-6
- xiv. R. M. Bozorth, 'Ferromagnetism', ISBN: 0-7803-1032-2
- xv. J. Clarke, A.I. Braginsky, 'The SQUID Handbook: Fundamentals and Technology...', ISBN: 978-3-527-60458-6

Figure list:

Figure 1. Logos of SPICA mission and SAFARI project. _____	6
Figure 2. Mission illustration from SPICA pamphlet (JAXA). _____	7
Figure 3. Illustration of magnetically and thermally shielded TES sensor array, made by: Henk van Weers _____	7
Figure 4. Illustration of a dipole, arrows indicate the direction of the field along the field line, source(http://en.wikipedia.org/wiki/File:VFPT_dipole_point.svg). _____	10
Figure 5. Illustration of (a) resistivity, (b) heat capacity, as a function of temperature comparing super- to conventional conductor material, source (http://users-phys.au.dk/philip/pictures/physicsfigures/). _____	11
Figure 6. Illustration of magnetic field penetration depth inside superconductors (type I & II), source: (http://www.doitpoms.ac.uk/tlplib/superconductivity/type.php) _____	11
Figure 7. Illustration of type II superconductor state diagram, source: (http://www.supraconductivite.fr/en/index.php?p=supra-levitation-phase-more) _____	12
Figure 8. Illustration of superconductive state as a function of magnetic field B, current density J and temperature T, source: (http://www.lhc-closer.es/1/4/8/0). _____	12
Figure 9. (a) Magneto-optical, (b) magnetic force microscope, imaged vortices in a type II superconductor where bright dots are high flux densities at the superconductor surface, source: (http://www.mn.uio.no/fysikk/english/research/groups/amks/superconductivity/vortex/index.html). _____	13
Figure 10. Illustration (from COMSOL) of magnetic flux density as color (blue=low to red=high) and arrow length, direction of the field is indicated by the direction of the red arrows. _____	14
Figure 11. Model (a) of dual Helmholtz coil setup (b), demonstrating homogenous field at centre of the xy-plane. _____	15
Figure 12. (a) Open cylinder superconductor example geometry, (b) simulated magnetic field distribution around superconducting open cylinder geometry. _____	16
Figure 13. 2D FEM flux density result (color coded) of superconducting boundary inside a current carrying finite solenoid. _____	18
Figure 14. (a) Illustration of (a) superconducting ring, (b) dc-SQUID or ring with 2 Josephson junctions. Source: (http://users-phys.au.dk/philip/pictures/physicsfigures/). _____	19
Figure 15. Simplified electronic circuit for feedback coil of a dc-SQUID. _____	19
Figure 16. Images of used cryogenic fluxgate(Bartington) setup, Mag-01H readout box with 3 type F probes. _____	20
Figure 17. Illustration of the equipment (not to scale) used when measuring with a SQUID at 4.2K (liquid He temperature). _____	22
Figure 18. Illustration of the Insert with SQUID probe mounted inside, this is our reference frame for moving the SQUID probe (a) through the solenoid or (b) niobium magnetic shield. _____	23
Figure 19. Image of dipstick part containing the '3D' SQUID. _____	24
Figure 20. (a) Illustration of laser modification for readout of z-axis rotation angle of the dipstick. (b) Image of the aligned laser modification on the 3D SQUID dipstick in the Insert. _____	24
Figure 21. Kelvinox 2 its Z-axis reference in room S.026, the 0° line in direction parallel to the windowed wall. (original by Caspar Bruineman) _____	25
Figure 22. (a) Illustration of the reference coordinate system of the SQUID inside Kelvinox 2. (b) SQUID position inside probe tip at 4 x-rotated positions, the x-axis is defined with the right-hand rule relative to the zy-plane. _____	25
Figure 23. Current amplifier circuit for solenoid, with R=330 Ohm. _____	26
Figure 24. Illustration of fluxgate magnetometer setup. _____	26
Figure 25. Phase-transition measurement setup with cryogenic fluxgate magnetometers. _____	27
Figure 26. (a) Design cross-section, (b) image, of point cooling modified setup. _____	28
Figure 27. Measured attenuation of closed Nb shield compared with a 2D COMSOL model of the setup. _____	29
Figure 28. Modelled geometry as measured on the Nb shield by Hereaus, on date: 24 January 2013. _____	30
Figure 29 COMSOL modeling profiles for flux confinement effect on B _z attenuation profile. _____	30

Figure 30. (a) COMSOL Model fitting measured solenoid profile, flux density B plotted as color. (b) COMSOL Model fitting attenuated signal profile, flux density in z -direction plotted as color. _____ 31

Figure 31. (a) Magnetic flux density in 2D plane of 3D Nb Shield model in COMSOL. (b) Magnetic field line profile by solenoid with 0.5° offset in z -axis, for radially equidistant field lines at $z=0$ (± 10 mm). 31

Figure 32. 3D model of $|B|$ fits for attenuation in B_z of closed Nb shield at an axis offset of 0.5° . ____ 32

Figure 33. Open optical entrance vs closed attenuation profile of flux density on z -axis, simulation results. _____ 33

Figure 34. 2D radial symmetric COMSOL model of opened optical entrance, with $D2_Nb=102$ mm. 33

Figure 35. (a) Different flux density trapped measured per fluxgate, due to solenoid radial B profile. (b) COMSOL model data for magnitude B as a function of distance r from z -axis. _____ 34

Figure 36. Magnetic field z -magnitude as a function of depth in cryostat, note the sudden drop to 0.0 at 77 cm. _____ 35

Figure 37. Images (a) top, (b) side view, of inside the shield sample (Hereaus), where a macroscopic crystal structure quality difference is observed between straight and curved niobium wall parts. ____ 35

Figure 38. Measured and modelled magnetic flux density profiles of 2 Helmholtz coils. _____ 45

Figure 39. Measured radial component in axial directed probe casing, measure of probe casing misalignment. _____ 46

Figure 40. Periodic VI curve of the dc-SQUID used for the attenuation measurements. _____ 47

Figure 41. Noise peaks presumably caused by a mobile telephone conversation, radio-frequent noise. _____ 48

Figure 42. Calibration of dipstick micro-meter for rotating SQUID in AC magnetic field. _____ 49

Figure 43. Solenoid in Kelvinox 2, measured maximum flux density at solenoid center in z -direction. 50

Figure 44. Log-scale plot of fluxgate measured dc-flux density and SQUID measured ac-flux density. _____ 51

Figure 45. Magnetic profile along z -axis as measured distance between tip of fluxgate and reference plate. _____ 52

Figure 46. Measurement 2 of the magnetic flux density B along the z -axis of the dipstick, overlaid with scaled model data from the simulation. _____ 53

Figure 47. Resulting Solenoid parameters from fitting 4 measurements on the flux density profile model. _____ 54

Figure 48. Attenuated flux density profile of solenoid by presence of Nb shield. _____ 55

Figure 49. Attenuation of closed cup shaped magnetic shield inside a solenoid, measured with an 0.1 Hz AC current. _____ 56

Figure 50. Fitted flux density B curves from delta B measurements with SQUID at different positions. _____ 57

Figure 51. Indicator of SQUID temperature measured as height from remaining liquid He layer. ____ 59

Figure 52. SQUID FLL response to rotation in steps of 14.3° , plotted per step. _____ 59

Figure 53. Illustration of Fluxgate sensor positions at edge of Nb closed shield, flux trapping transition measurement setup. _____ 60

Figure 54. Measured magnetic flux density $|B_z|$ as a function of depth inside the Kelvinox II cryostat. 61

Figure 55. Flux density (remnant flux corrected) B_z as a function of depth Z , temperature T and current I . _____ 62

Figure 56. Active magnetic field nulled transition, where fluxgate # 1266 went through T_c before # 1265. _____ 63

Figure 57. Measured (KII remnant + solenoid) magnetic flux density as a function of depth of measurement setup bottom below KII valve. _____ 64

Figure 58. In-field cooled measurement data, with annotated temperature dependent hysteresis in depth. _____ 65

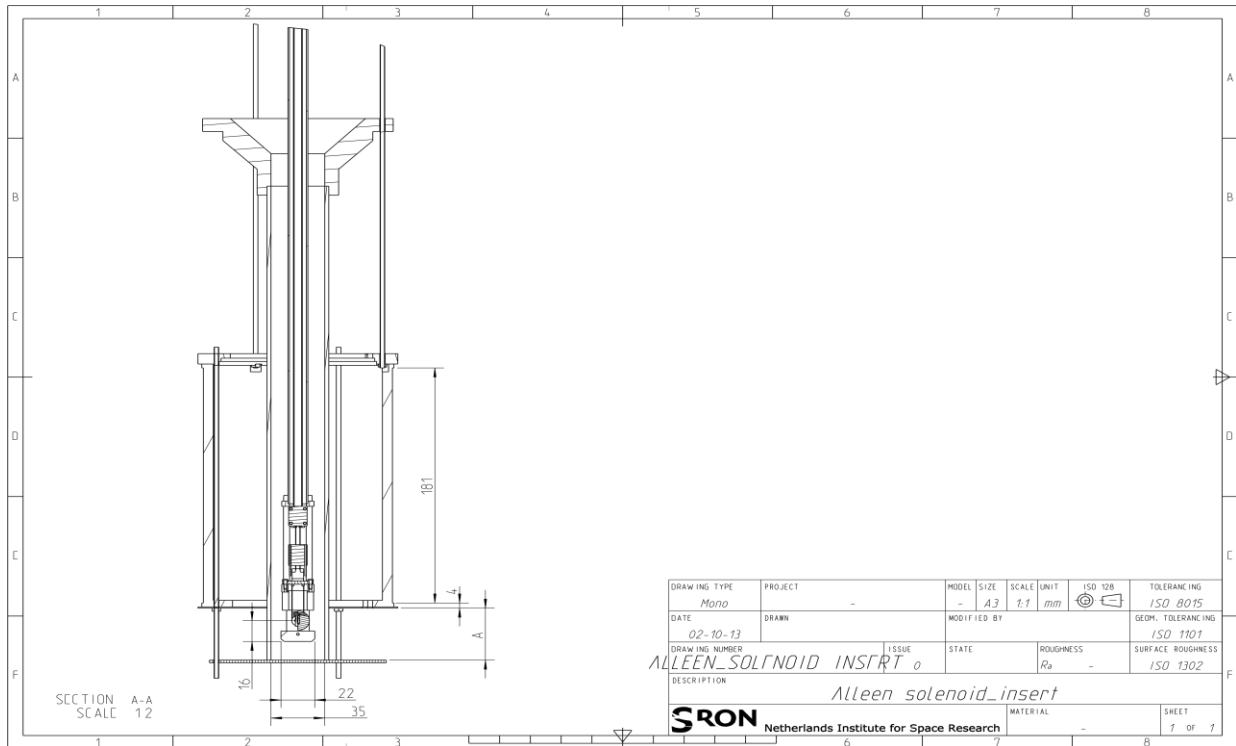
Figure 59. Resulting flux expulsion visible as a sudden decrease from expected remnant field (~ 100 nT). _____ 65

7 Appendix A: Technical designs

Here technical designs for the measurement equipment (setup) from ED (engineering department) are given. The measurement setups were built to these technical specifications.

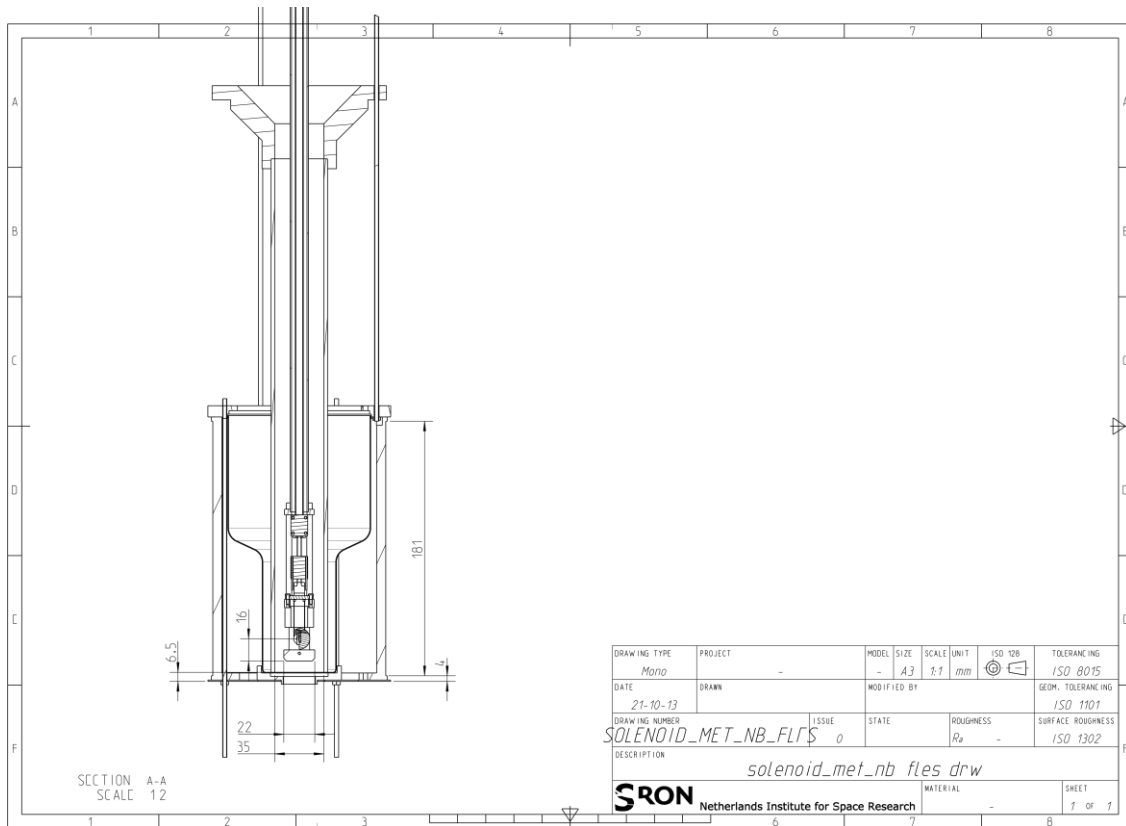
7.1 Insert with solenoid

The bottom part that is brought into the cryostat is illustrated, a solenoid coil is wound around the 181 mm length cylinder.

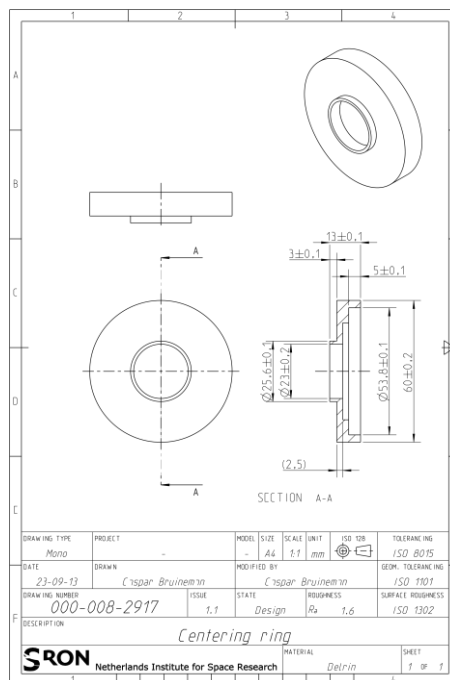


7.2 Insert with Nb closed shield

Inside the solenoid holder the closed Nb shield (manufactured by Hereaus) is fitted. A centring ring at the bottom is holding the Nb shield in place.

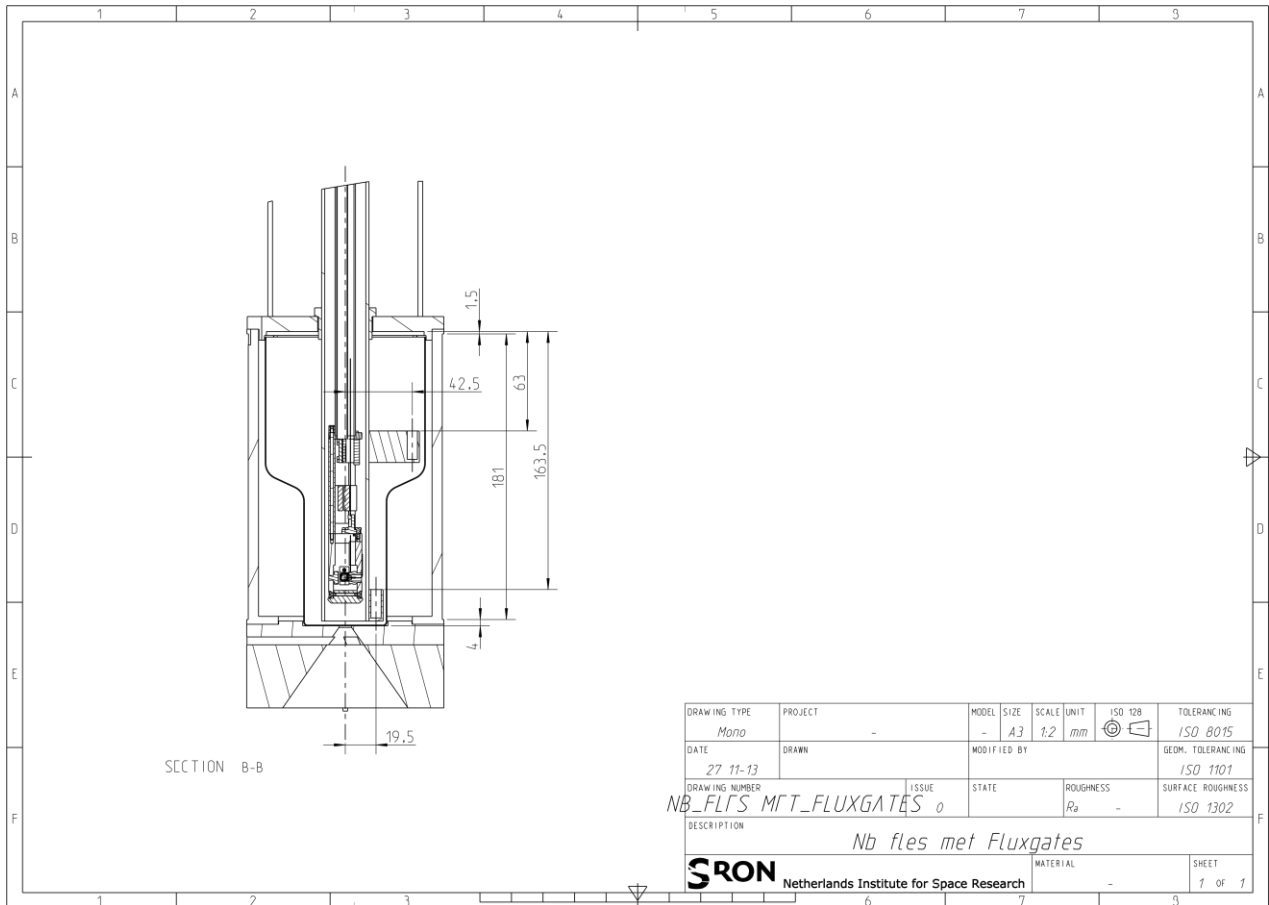


A separate technical illustration of the shield holder (Centering ring) is given.



7.3 Nb shield with Fluxgate sensors

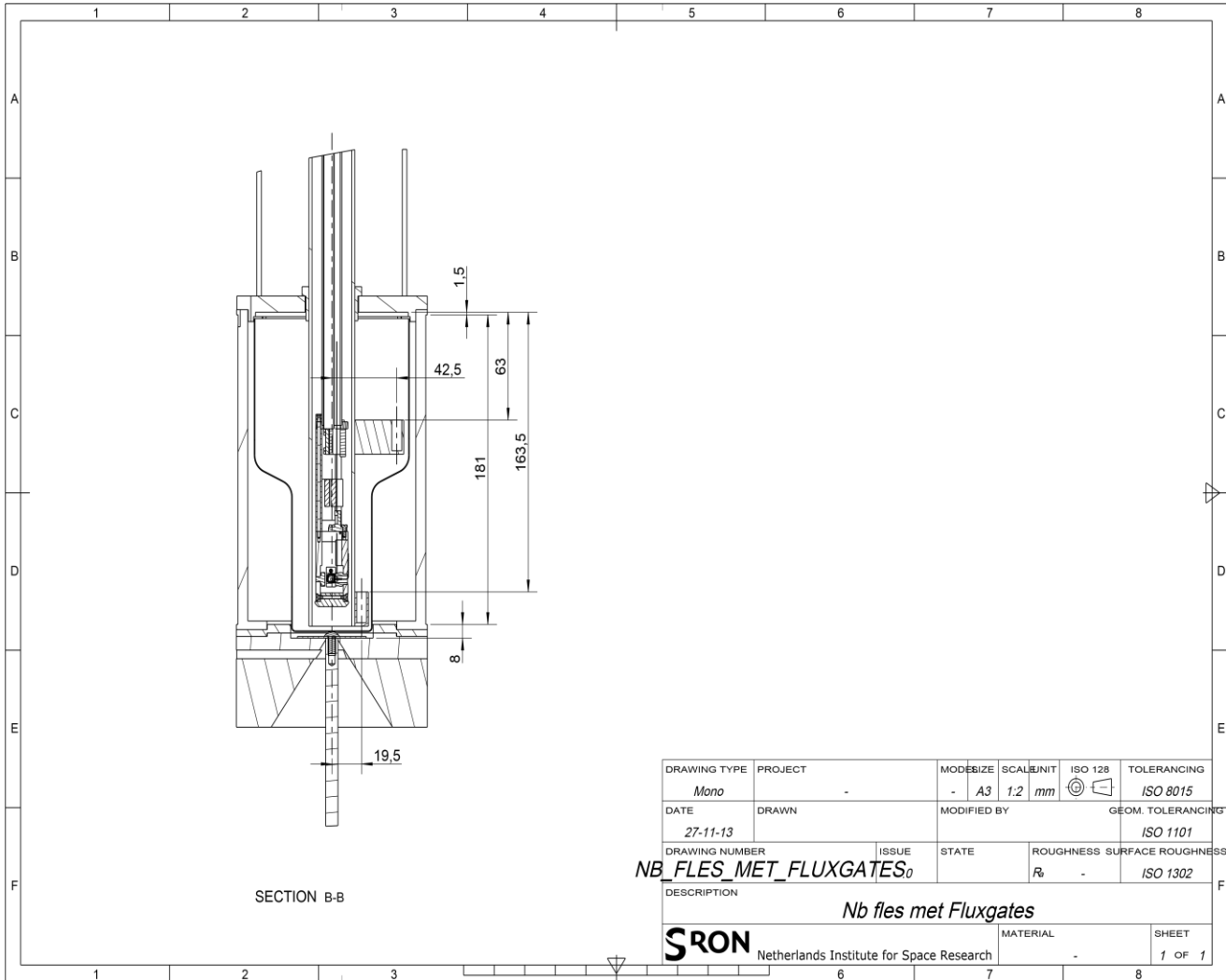
The fluxgate measurement setup's technical drawing is given.



The height of the He vapour channelling cone (on the bottom of the Insert) was measured to be 40 ± 0.5 mm for the bottom part, 13 ± 0.5 mm for the middle part (with narrow opening to the Nb shield).

7.4 Point cooling (modification)

A modification is made (on 7.3) to make cooling from a point in the shield bottom possible. With a copper rod going down through the opening to the bottom of the shield.



8 Appendix B: Measurement reports

In this chapter each of the required* measurements is summarized and the derived results are given.

**Calibration of equipment*

Calibration and verification of the PTB ($7\text{nT}/\phi_0$) dc-SQUID including:

- finding of optimal I_{bias} and V_{bias} values,
- measuring linear flux lock loop response for flux B as a function of current I_ϕ .

Cryostat (Kelvinox II) remnant field characterization.

Calibration of the dipstick including measurements of:

- the height of the centre of the SQUID as a function of height of the dipstick from the reference plate,
- rotation angle of the SQUID around the x-axis as a function of micro-meter setting, investigating possible hysteresis and mechanical slip,
- magnetic field B_z profile as a function of SQUID height z in the solenoid (without shield),
- maximum magnetic field B_z as a function of solenoid current $I_{solenoid}$, where a linear relationship is expected from theory.

Fluxgate magnetometer calibration to validate SQUID measurements including:

- magnetic field B_z profile as a function of fluxgate height z in the solenoid,
- maximum magnetic field B_z as a function of solenoid current $I_{solenoid}$, where a linear relationship is expected from theory,
- measured flux of a transvers (radially) applied field in Helmholtz coil as a function of rotation of sensor casing.

Helmholtz coils setup calibration including:

- precise measurement of coil dimensions,
- magnetic flux density profiles along axis of both inner and outer Helmholtz coils.

**Measurements of interest*

Magnetic attenuation measurement of shield sample including:

- attenuated magnetic field B_z profile as a function of z in the solenoid,
- maximum attenuated magnetic field B_z as a function of solenoid current $I_{solenoid}$, where a nonlinear relation is expected around the critical field B_C ,
- finding residual magnetic field vector directions inside the shield by rotation of the dipstick and dc-SQUID.
- Flux trapped residual DC field measurement, cool down shield with solenoid applying a field of $\sim 100 \mu\text{T}$.

Phase transition measurement including:

- Magnetic flux trapping of Nb shield during in field cooling,
- Proof of concept experiment for in-field cooling technique (for expulsion of flux).

8.1 Helmholtz x and y axis B profile

A measurement of the magnetic field homogeneity inside the dual Helmholtz setup, both x-axis (outer coils) and y-axis (inner coils) have been scanned with fluxgate 1266. This measurement is done in preparation of the warm attenuation measurement of the Cryoperm shield that will be placed inside these dual coil sets.

8.1.1 Method

A guide tube was mounted axially inside the Helmholtz setup, through this tube a fluxgate mounted inside a tightly fitting guide rod was moved along the axis of the Helmholtz coil. An offset of 223.3 mm was measured for the fluxgate sensor centre and the inner coils centre, for the outer coils this was 221.5 mm.

8.1.2 Result

See Figure 38 for a plot of measured points and COMSOL model data fitting or analytical formula prediction from geometry. The linear change in measured B indicates a ferromagnetic material moving along in the scanning direction x or y .

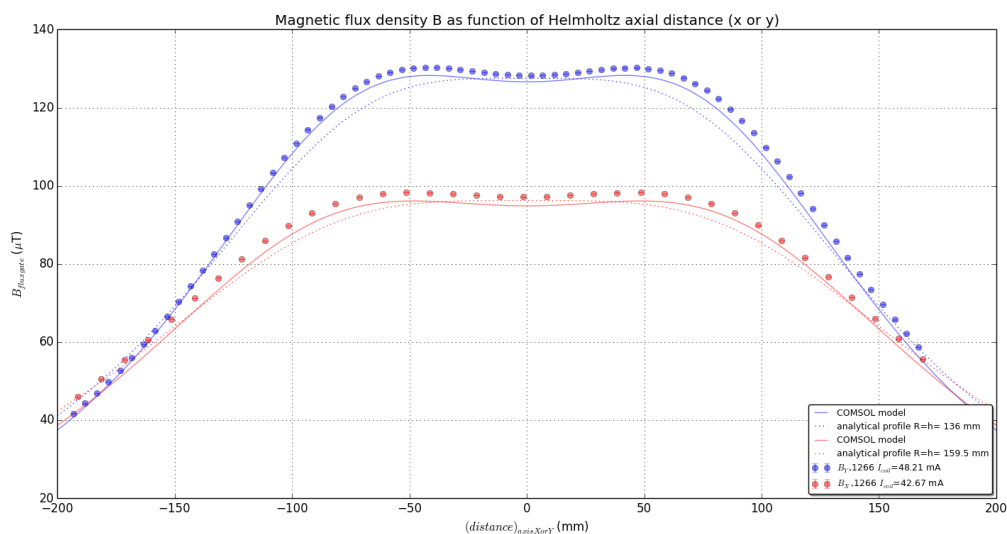


Figure 38. Measured and modelled magnetic flux density profiles of 2 Helmholtz coils.

8.2 Fluxgate sensor characterization

The three Bartington fluxgate sensors 1265-1267 were delivered calibrated with an accuracy of 2 nT for absolute flux measurements. The direction in which this fluxgate was most sensitive was specified as $\Delta\theta_{\text{axis}} < 0.2^\circ$ from the cylindrical holder, with an accuracy of 1%.

8.2.1 Method

This was checked by measuring the flux of an transverse applied field under rotation of the fluxgate holder. The amplitude of the periodic signal corresponds to the angle the sensing direction makes with the x-axis of the cylinder.

8.2.2 Result

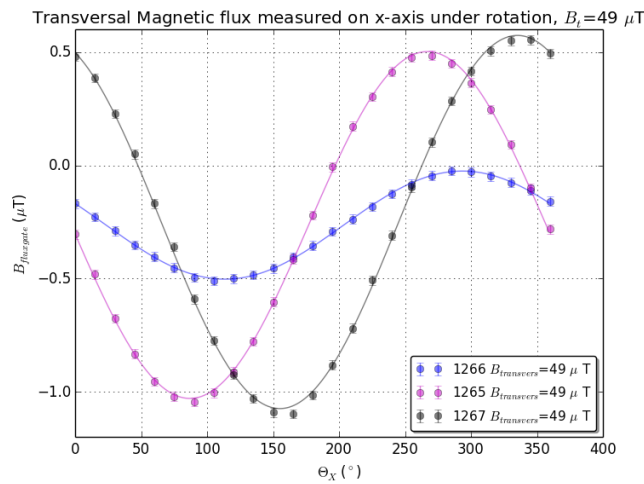


Figure 39. Measured radial component in axial directed probe casing, measure of probe casing misalignment.

The fraction of the periodic amplitude seen in Figure 39 over applied transversal flux allows the angle of misalignment to be calculated as $\theta_{offset} = \sin^{-1}(B_{periodic}/B_{transversal})$

Probe 1266: $\frac{B_{periodic}}{B_{transversal}} = \pm 0.5\%$ or an angle of $1' 8''$ ($0.3^\circ \pm 0.6^\circ$ when rounded up). Case diameter of 6 ± 0.05 mm,

Probe 1265: $\frac{B_{periodic}}{B_{transversal}} = \pm 1.6\%$ or an angle of $3' 36''$ ($0.9^\circ \pm 0.6^\circ$ when rounded up). Case diameter of 5.9 ± 0.1 mm,

Probe 1267: $\frac{B_{periodic}}{B_{transversal}} = \pm 1.7\%$ or an angle of $3' 53''$ ($1.0^\circ \pm 0.6^\circ$ when rounded up). Case diameter of 6.1 ± 0.05 mm.

A maximum systematic error could be expected by the mismatch of sensor holder and PVC centering tube of $\frac{\Delta radius}{length} = \pm 1\%$ or an angle of $\pm 0.6^\circ$, also the fluxgate sensor casing and sensor holder radii had a similar maximum systematic error. Therefore probe 1265 and 1267 appear to have a more significant deviation between casing and axis of probe than specified by the manufacturer. *1266 had a Duplo measurement after increasing the setup radius, here an error of $\pm 1.1\%$ or angle of 0.6° was measured. *Duplo 1267: $\pm 2\%$ and angle of 1.2° .

8.3 dc-SQUID (3d-SQUID) amplified response & noise level

8.3.1 Method

The SQUID in amplification mode was biased with voltage $V_b = 162$ mV and current $I_b = 11.8$ μ A, causing it to walk with a nonlinear response to the change in B . The feedback coil was used to generate a flux of 7 nT, requiring a current of 16.8 μ A. The SQUID response as a function of the feedback coil current should show a sinusoidal like function. This was measured using a DAC with 2 channels, channel 1 for the input signal and channel 3 for the SQUID output.

8.3.2 Result

Given is the periodic nonlinear (also known as ‘walking’) response of the dc-SQUID.

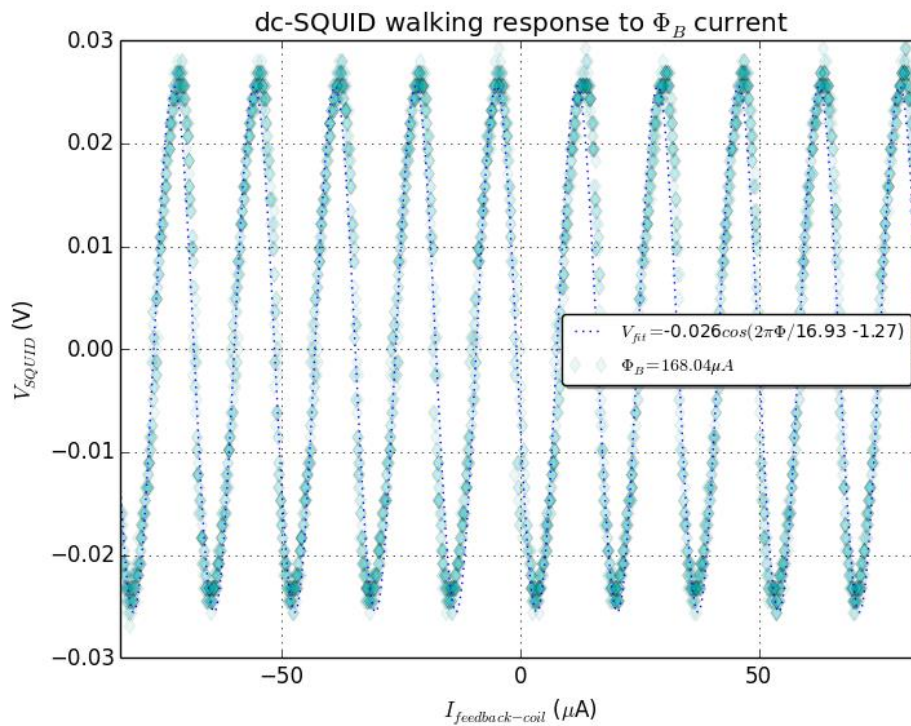


Figure 40. Periodic VI curve of the dc-SQUID used for the attenuation measurements.

As can be seen in Figure 40 the actual response does not exactly fit a sinusoidal function as expected, the fitted $I_{\phi_B}/\phi_0 = 16.93 \mu\text{A}$, while this one was estimated to be $16.8 \mu\text{A}$ from the 10 periods counted over a triangle signal with $I_{feedback-coil} = 168 \mu\text{A}$. This estimation corresponds to the literature value ($16.8 \mu\text{A}$) given by manufacturer PTB. The peak to peak amplitude of the SQUID response was found to be 51.1 mV at current biasing settings. According to manufacturer PTB each ϕ_0 corresponds to a flux of $7 \pm .2\% \text{ nT}$, this is assumed to be correct during the following measurements. The area of the PTB dc-SQUID would be expected to be $\phi_0/S_\phi \cong 2.95 \cdot 10^{-7} \text{ mm}^2$.

The noise level measured here is limited by the read-out electronics, like the DAC or oscilloscope resolution, this had a peak to peak amplitude of 10 mV or $\sim 3 \mu\text{A}$ with a feedback resistance setting $R_f = 30 \text{ k}\Omega$.

8.3.3 RF-noise from nearby sources

To prevent radio frequent noise in the SQUID, it must be kept in a faraday cage. Any nearby electronics or computers will also cause electromagnetic noises in the detectable bandwidth of the SQUID. [xv]

An example is given in Figure 41 where a telephone was within 5 m of the SQUID whilst measuring its VI-curve. The expected VI-curve without noise can be seen in Figure 40.

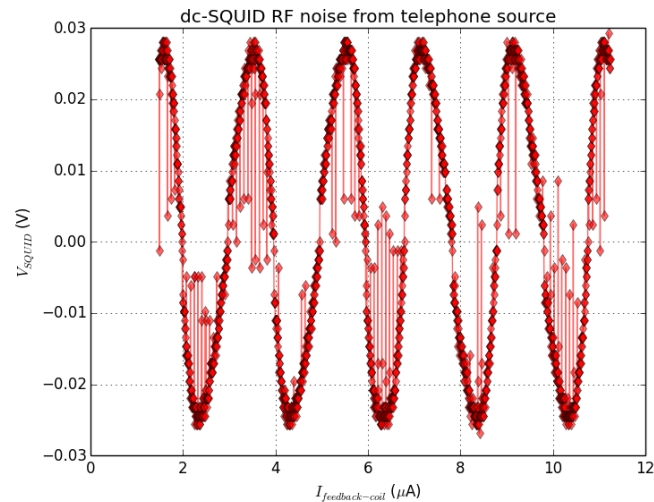


Figure 41. Noise peaks presumably caused by a mobile telephone conversation, radio-frequent noise.

Here the SQUID was already inside a completely metal container (Kelvinox 2 cryostat), surrounded by a high magnetic permeability metal.

8.4 SQUID rotation around x-axis

Here a series of measurements is done to investigate a possible slip on the micro-meter transfer and measure the hysteresis on the rotation.

8.4.1 Method

The SQUID is placed right at the centre of a rotatable plane. This plane on the low end of the dipstick can be rotated using a micro-meter on the top of the dipstick. Measurements have been made of rotating the micro-meter while the solenoid provided an AC magnetic field along the z-axis. Hysteresis in the micro-meter is characterized by finding the offset between the data points.

8.4.2 Result

A calibration constant of $14.3 \pm .3(^{\circ}/\text{mm})$ or 0.25 ± 0.005 (rad/mm) for the micro-meter has been fitted to the second measurement and the hysteresis measurement.

The first measurement showed signs of a measurement error due to hysteresis, this was confirmed with a hysteresis measurement of the second measurement over a greater range of the micro-meter.

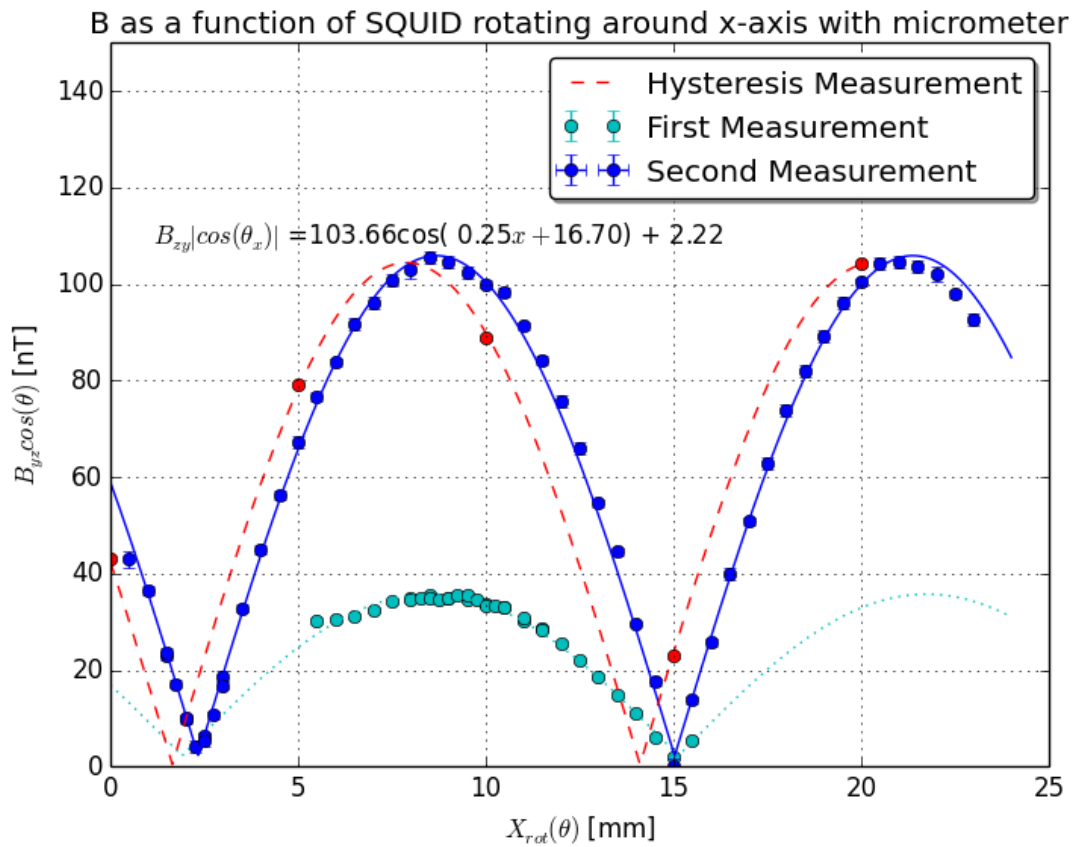


Figure 42. Calibration of dipstick micro-meter for rotating SQUID in AC magnetic field.

$I_{sol1} = 20.15 \text{ mA}$, giving an expected $B \approx 52 \text{ nT}$, B is calculated using the following linear translation of readout SQUID FLL voltage: $R_f = 10 \text{ k}\Omega$, $M_f = \frac{1}{16.8} \phi_0 / \mu\text{A}$, $S = 7 \frac{\text{nT}}{\phi_0} \pm 0.3\%$, used in equation (19). $I_{sol2} = 40.29 \text{ mA}$.

8.5 Low frequent AC solenoid flux

8.5.1 Method

For different solenoid currents the measured approximately maximum magnetic field is expected to increase proportionally with the current. As the SQUID is not an absolute magnetometer a low frequent AC signal was used, where the peak to peak values of the current and SQUID response were taken.

The induced current in the dc-SQUID in flux locked loop mode is read out and linearly translates into flux.

8.5.2 Result

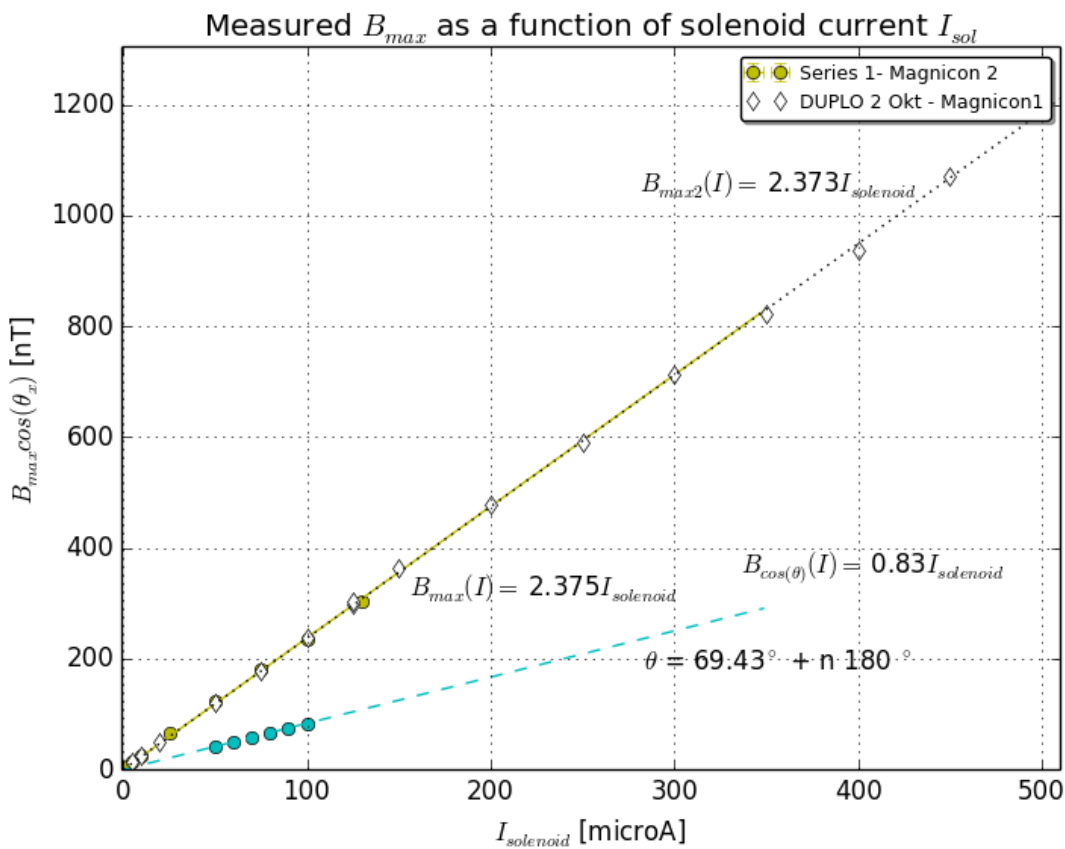


Figure 43. Solenoid in Kelvinox 2, measured maximum flux density at solenoid center in z-direction.

The measured flux density B_z is found to be linearly related to the current $I_{solenoid}$ with a constant factor of $2.37 \pm .01 \text{ nT}/\mu\text{A}$. If the SQUID is rotated around its x-axis, a smaller component of this signal is measured, defined by $|\cos(\theta)|$ of the angle θ the SQUID is rotated out of the z-axis direction. Thus no signal can be measured at $\theta = \pm 90^\circ$, maximum signal at $\theta = 0^\circ$ or 180° with respect to the z-axis.

8.6 Solenoid dc-flux

8.6.1 Method

A fluxgate magnetometer is used at room temperature on an aluminium rod placed at the centre of the solenoid coil (113.5 mm from bottom reference guide-tube) to measure the difference in constant flux at the point of the fluxgate tip. The tip was aligned with the z-axis, but the angular offset between the actual measured vector component is to be determined through calibration.

The same type of current source was used for all 4 measurement series, namely the magnicon 1 or 4 current source. 1&2 used the magnicon 4 to control the SQUID and solenoid current, the DUPLO 2 and fluxgate measurement used the magnicon 1 as current source.

8.6.2 Result

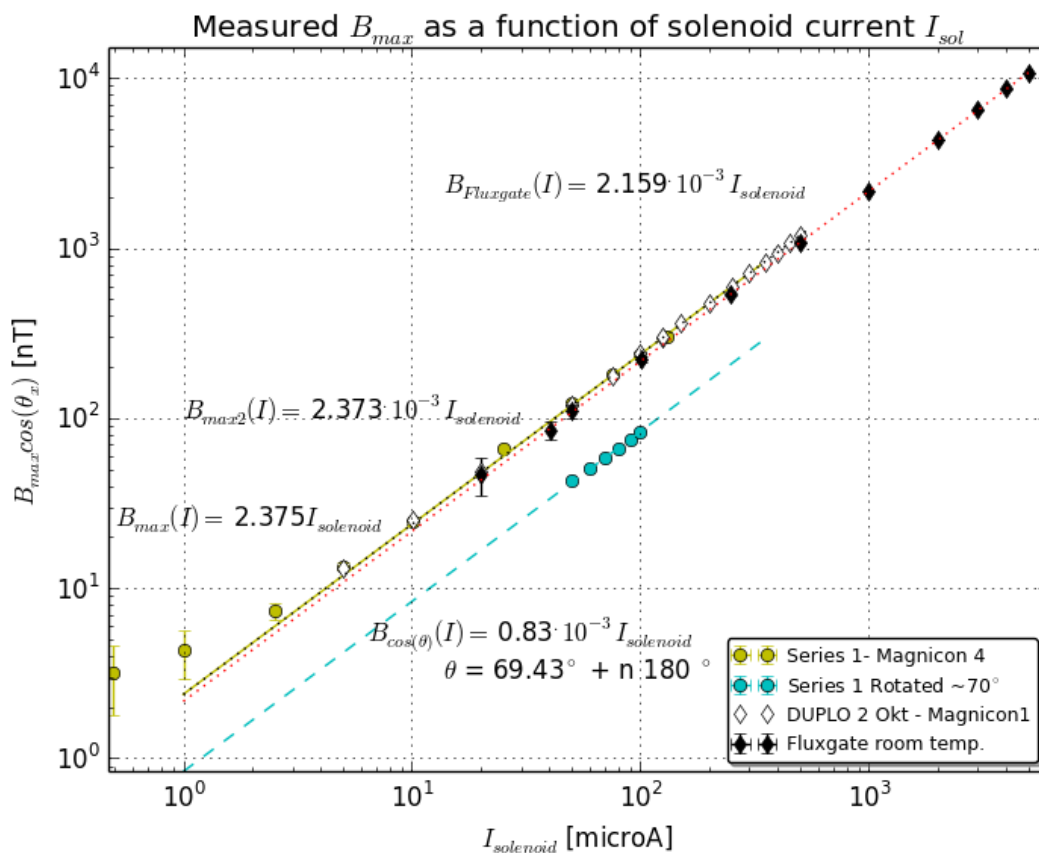


Figure 44. Log-scale plot of fluxgate measured dc-flux density and SQUID measured ac-flux density.

Resulting slope of the fluxgate measurement in Figure 44 indicates a flux density inside the solenoid of $2.159 \pm .002$ nT/ μ A, the expected solenoid flux density from SQUID measurements was $2.374 \pm .002$ nT/ μ A. This $\sim 10\%$ difference is larger than the possibly 2% error in sensitive direction of the fluxgate, unknown position of coil inside the fluxgate tip or a difference in solenoid size due to measuring at room temperature. Further measurements with the fluxgate magnetometer at the same cryogenic temperature will resolve this issue.

8.7 Measured flux density as a function of fluxgate position

8.7.1 Method

The fluxgate its sensitive tip was aligned with an aluminium rod ($\mu_r = 1.000022$) to introduce a minimal measurement error compared to using an aluminium dipstick as a mount for the magnetometer.

8.7.2 Result

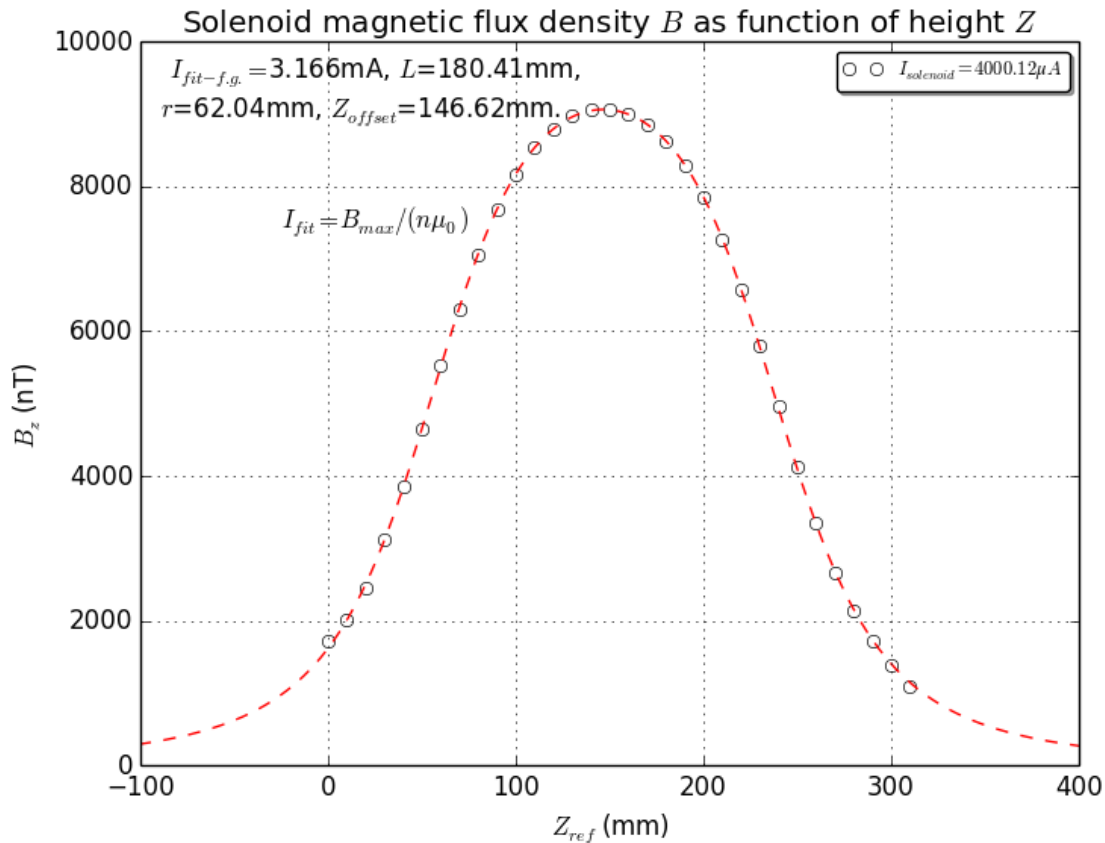


Figure 45. Magnetic profile along z-axis as measured distance between tip of fluxgate and reference plate.

The profile parameters in Figure 45 show that again a solenoid length within 181 ± 1 mm is found, where the centre would be at 90.5 mm. This result shows in an offset of the measuring point inside the tip of $17.5 \pm .5$ mm, this is about halfway the 33 ± 1 mm cylindrical fluxgate container.

8.8 Measured flux density as a function of SQUID height

8.8.1 Method

A 0.2 Hz signal with an current of $I_{peak-peak}$ is applied on the solenoid to generate a magnetic field.

With the SQUID rotated within $\sim 5^\circ$ of the maximum B_z signal the dipstick is lifted from the reference plate. The distance from this reference plate is measured on the outside of the Insert.

8.8.2 Result

The reference $B(z)$ curve of the solenoid has been measured with the SQUID magnetometer. In Figure 46 the point measurements are plotted over the COMSOL model curve of the solenoid.

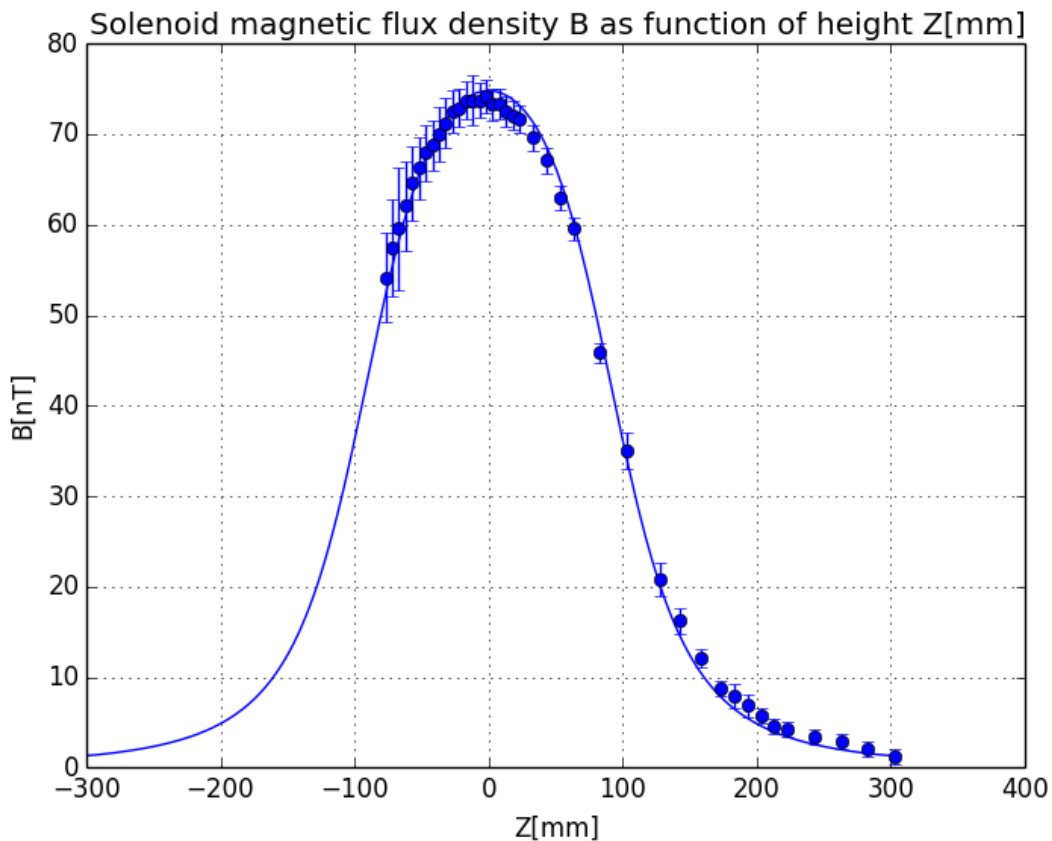


Figure 46. Measurement 2 of the magnetic flux density B along the z -axis of the dipstick, overlaid with scaled model data from the simulation.

The data points were taken with a 0,0 mm reference point at the bottom plate, with this overlay an offset of the maximum has been estimated to be 77 mm above the bottom plate, in contradiction to the mechanically expected $90.5 + 38.25 - 16 = 114$ mm. For a linearly scaling solenoid current with the maximum flux, the solenoid current is estimated from a COMSOL simulation $I_{solenoid} = 30 \pm 2 \mu A$. The applied AC current on the solenoid was $30.5 \mu A$ from peak to peak. Giving a linear scaling factor for the solenoid of 2.6 A/mT, where the model predicted a scaling factor of 2.4 A/mT. Both fall within the value of $2.5 \pm .1$ A/mT.

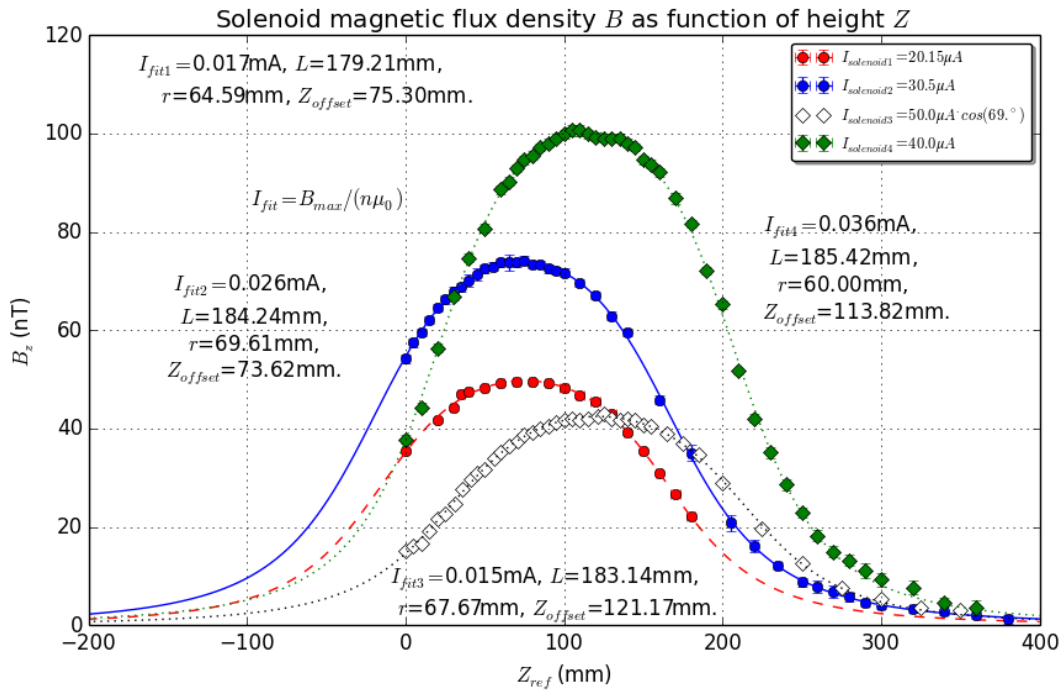


Figure 47. Resulting Solenoid parameters from fitting 4 measurements on the flux density profile model.

The results from fitting two $B(z)$ measurement series were obtained by using equation (7) for the approximate current I_{fit} through the solenoid and equation (8) for the solenoid length, radius and offset from lowest measurable point in the Insert (see Figure 18).

An offset for the peak intensity of the solenoid field along the z-axis has been found to be 74.5 ± 1 mm above plastic shield holder. For measurement 1&2 the reference point was positioned at a distance $z_{sol} = \sim 0 \pm 2$ mm from the start of the solenoid, where the SQUID was positioned at a distance $z_{SQUID} = 16.0 \pm .2$ mm from the plastic obstacle in the dipstick.

For a solenoid with length $L = 181$ mm, the maximum magnetic field density would be expected at $\frac{L}{2} = 90.5$ mm, the mechanical offset of the SQUID to the bottom plate added to the retrieved offset should add up to this expected distance along the z-axis: $Z_{offset} + Z_{SQUID} = L/2$. This is the case for the measurements in Figure 47.

Measurement 3 was done at an angle of 69° rotated around the x-axis with the micro-meter, this allows to check if the field lines at the position of the SQUID run along the z-axis.

Measurement 4 shows an offset of the reference 0.0 mm point of 113.8 mm, this was expected to be 113.75 mm from the measurable depth improvements made to the Insert.

8.9 Shield's magnetic attenuation

In this measurement a low frequency AC signal was used to retrieve the attenuated response of the closed Nb shield.

8.9.1 Method

Again an alternating current signal is applied to the solenoid, but here there will be a superconducting magnetic shield in between the windings of the coil and the magnetometer. The z-axis component of a low frequent B field produced by the solenoid is measured.

The attenuation is a (unitless) measure of the fraction of the magnetic field amplitude that was reduced by the presence of the shield.

8.9.2 Result

The measured magnetic flux profile compared to the calibration profile of the solenoid is given in Figure 48, where there is an offset of $Z_{SQUID} - Z_{ref} = 16.0$ mm in z-direction for both measurements and the solenoid starts at $Z_{sol} = (39.25 \pm .5)$ mm relative to Z_{ref} .

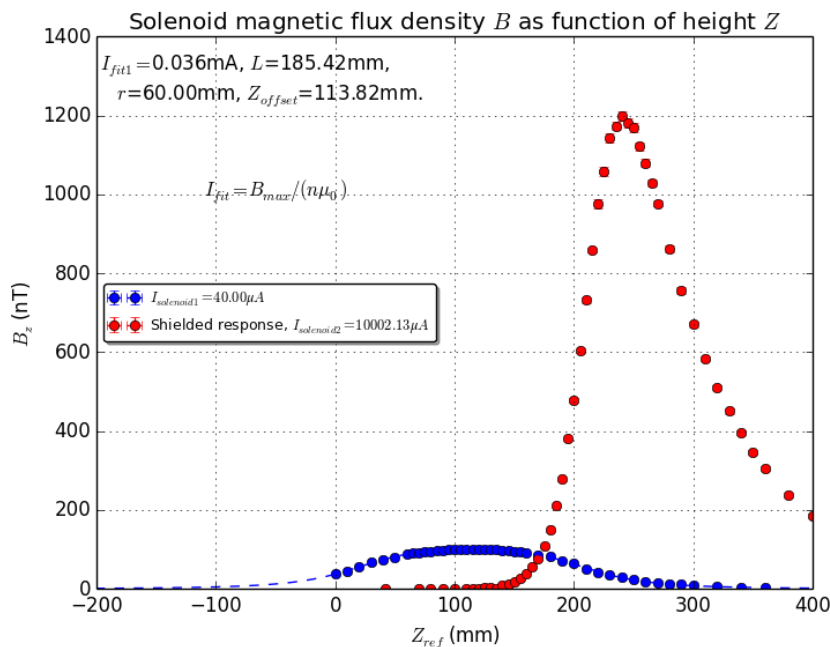


Figure 48. Attenuated flux density profile of solenoid by presence of Nb shield.

The attenuation A found for the first 100 mm inside the closed superconducting shield is of the order of 10^5 (amplification factor of 10^{-5}), or even more attenuated as the signal was smaller than the noise on the SQUID.

Additional measurement series with a larger ($B_{max\ 03} = 92.37\ \mu\text{T}$) applied magnetic flux from the solenoid allowed the attenuation to be measured with higher accuracy at the bottom of the cup shield. These data series are plotted on a logarithmic y-scale in Figure 49.

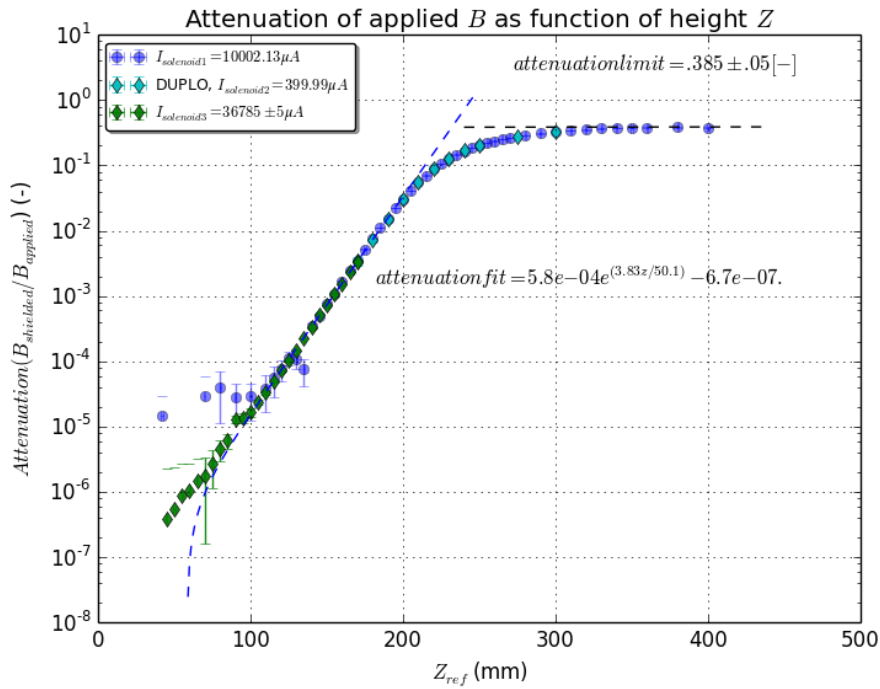


Figure 49. Attenuation of closed cup shaped magnetic shield inside a solenoid, measured with an 0.1 Hz AC current.

It is noticed that the attenuation does not converge to unity high above the solenoid, this is only expected for a shield in a homogeneous field. The slope of the attenuation is expected to follow an exponential function, this measurement shows a slope of factor $\frac{\sim 1 \cdot 10^3}{100}\text{ mm}^{-1}$.

8.10 Residual magnetic field vectors

Here the residual magnetic field was measured of a ‘zero field’ trapped measurement. This is mostly the earth’s magnetic field after attenuation by the μ -metal surrounding the cryostat.

8.10.1 Method 1

With the SQUID its x-axis positioned both at $(0 - 7.5)^\circ$ and $(90 - 7.5)^\circ$ both components of the DC residual field can be measured by rotation of the x-axis by the micro-meter on the 3D-dipstick. Due to the unreliable FLL mode response, relocking is required after each measurement, the delta or difference in signal through the solenoid is measured and should be sinusoidal over the rotation of the x-axis or z-axis according to equation

(22).

$B(\theta) = B_0 \cos(\theta)$, therefor the following formula is valid for this data: $\frac{dB(\theta)}{d\theta} = -B_0 \sin(\theta)$, both are plotted in Figure 50.

8.10.2 Result

The setup with the closed Niobium shield was used to measure the residual/trapped field vector at a height $Z_{ref} = 100$ mm, scanning 2 perpendicular planes of \vec{B} to obtain the vector.

An expected angle on the xy-plane for the vector projection on xy is $(117.5 \pm 5 + n \cdot 180)^\circ$ from the direction of the x-axis (0°) at 100 mm height.

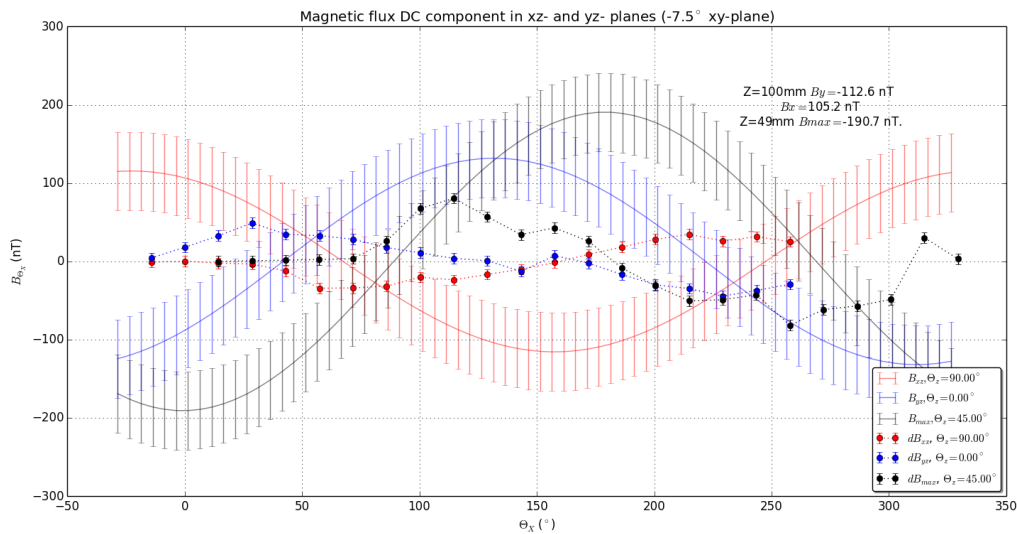


Figure 50. Fitted flux density B curves from delta B measurements with SQUID at different positions.

A maximum DC-field has been found in the order of $2 \cdot 10^{-7}$ T, that was trapped in the radial direction inside close to the bottom of the shield at $Z_{ref} = 42$ mm.

If this remnant flux would pass through the Nb shield in an orderly triangular lattice, the spacing between the vortices would be $a \cong 0.1$ mm, according to equation (6).

8.10.3 Method 2

Rotating the SQUID around the z-axis by turning the Insert and using the micro-meter to rotate around the x-axis, the magnetic field vector and magnitude can be retrieved for various points along the z-axis. This allows an experimental check of possibly trapped fluxes in the superconducting magnetic shield, most likely in the more curved parts of the cup.

Alternative suggestion: Using fluxgate magnetometers that can be rotated towards the internal edges of the Nb shield after the probe is inserted in the Insert. + Absolute measurement, - less sensitivity.

8.11 Trapped magnetic field vectors

A trapped magnetic flux in the superconducting shield could have negative effects on the nulling of the magnetic field, required for the TES detectors to operate at highest sensitivity. This measurement is done to test if a single body part can trap flux inside the detector area and to investigate the magnitude and direction of this possibly trapped field.

8.11.1 Method

*Cooling down the Nb closed cup shield with a DC magnetic field applied using the solenoid. If the magnitude is significantly different from the residual field measured an extra flux has been trapped by the presence of a DC field during cool down. Fluxgate detectors are preferably used for these absolute flux measurements.

'Field cooled measurement of the Niobium stepped shield:

1. *Raise the superconducting coil + Niobium shield + SQUID probe in the Kelvinox to a level at which you are sure the Niobium shield is not superconducting.*
2. *At this temperature apply a constant current to the coil to generate a magnetic field of 100 microTesla. With the current running (and thus applied B-field) lower the shield + coil + SQUID probe assembly to a level it is completely superconducting.*
3. *At the low temperature remove the external current applied to the superconducting coil.*
4. *Let the setup settle for a while (10 minutes, cup of coffee, for example). This to allow any transients to damp out.*
5. *After this delay start measuring the static magnetic field inside the Niobium as a function of z coordinate.'*

Points of interest to investigate for trapped flux are the more bend parts of the shield: the curved transition between both radii, the bottom edge of cup.

Measuring the temperature of the shield is done indirectly by the SQUID probe. Since the SQUID is also made of Niobium, it roughly has the same transition temperature $T_c = 9.22\text{K}$, monitoring the amplified mode response as seen in Figure 40 will allow the temperature to be determined in the range of $4.2 < T < 9.2\text{K}$. If the response reduces to 0 mV the probe will be above its transition temperature.

8.11.2 Results

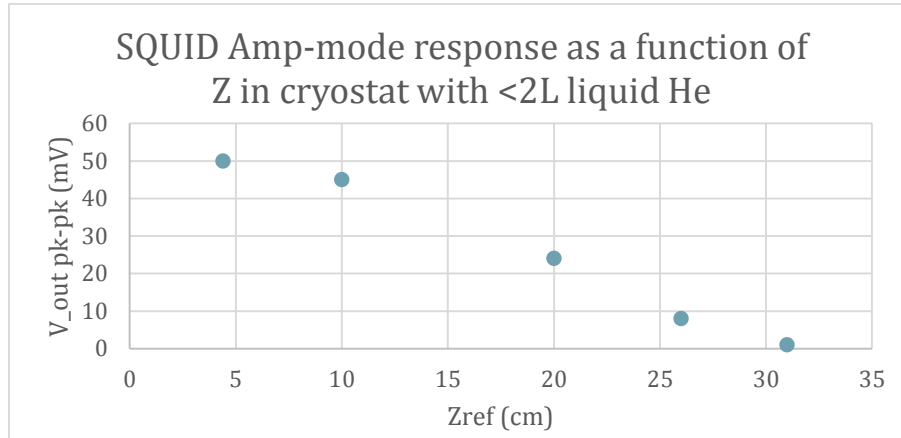


Figure 51. Indicator of SQUID temperature measured as height from remaining liquid He layer.

It can be seen that there is a relation to the temperature and the amp-mode response if a temperature gradient from the bottom to the top of the cryostat is assumed to be present.

Superconducting Nb has a reduced critical current density at higher temperatures ($J_c \rightarrow 0$ at T_c). This indicator is used to determine when the Nb shield would be above its transition temperature, with the SQUID probe at the bottom of the closed shield. A peak to peak amp-mode response of 65 mV is measured in a filled cryostat for this SQUID.

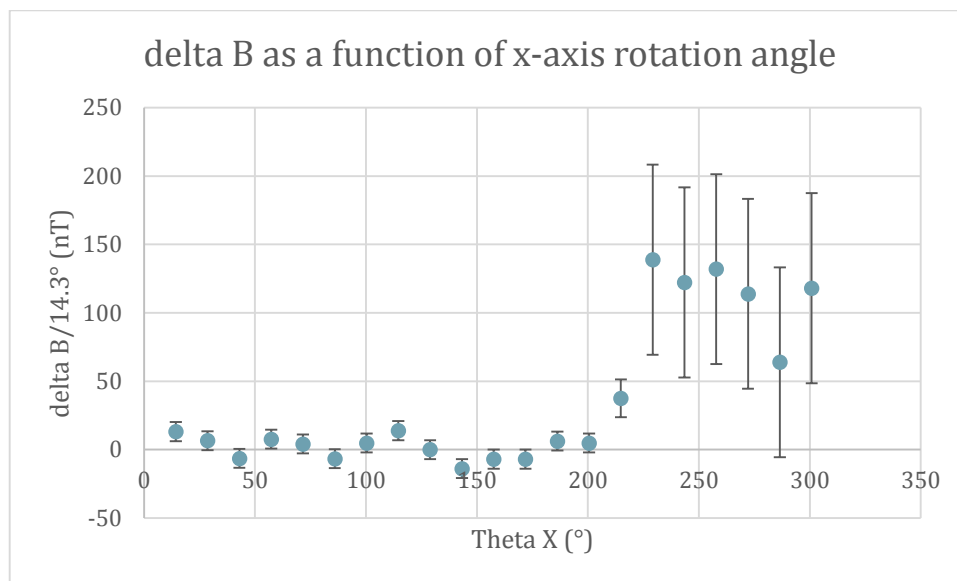


Figure 52. SQUID FLL response to rotation in steps of 14.3°, plotted per step.

The measurement results plotted in Figure 52 do not show an expected sinusoidal response $B \cos(\theta)$. Also no conclusion was drawn from this measurement due to the large error when doing a summation of the data points.

8.12 Phase transition (Meissner state) measurements

To investigate the absolute flux trapped during cool down through $T_c = 9.22$ K near high flux density surfaces in closed Nb shield design.

8.12.1 Method

Monitoring the Nb shield during the superconducting transition is only possible with cryogenic fluxgate sensors. By using 2 fluxgate sensors at different positions in the shield area of interest can. A magnetic field (via solenoid current) can be applied to the Nb shield, where the measured flux at the fluxgates will vary accordingly as long as $T > T_c$. When $T < T_c$ one of the two fluxgates (or both) will detect a higher (less decreased) magnetic flux $B_{trapped}$ on top of the residual field in the sensing direction. The ratio between $B_{applied}$ and $B_{trapped}$ will indicate the initially cooled through T_c area fraction of the total area perpendicular to the solenoid magnetic field, because the Meissner effect takes over at a temperature just below T_c in the presence of a magnetic field.

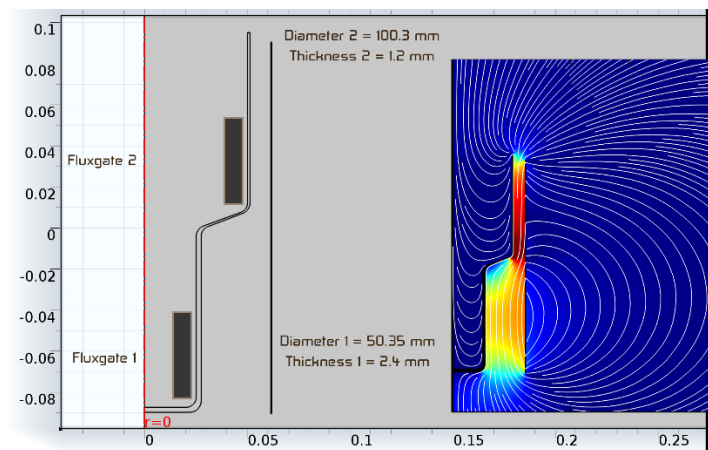


Figure 53. Illustration of Fluxgate sensor positions at edge of Nb closed shield, flux trapping transition measurement setup.

The difference in area of trapped flux is factor ~ 4 ($r_2 \cong 2 r_1$), thus a factor ~ 4 lower flux is expected to be trapped when bottom area transits to the Meissner state before the top edge does.

8.12.1 Result

Fluxgate 1 position: $R_1 = 19.5$ mm, $Z_1 = -71.5$ mm, fluxgate 2 position: $R_2 = 42.5$ mm, $Z_2 = 28.5$ mm, where all distances are given relative from the solenoid centre (or z-axis).

With a solenoid current of $I = 5.000$ mA a magnetic flux density in +z-direction was measured of $B_{z1} = -8.29 \pm .05 \mu\text{T}$ (fluxgate 1) and $B_{z2} = -11.05 \pm .05 \mu\text{T}$. Note that the sensing coil wires changed polarity and that in this setup the downward pointing fluxgates give the measured field in upward direction as positive instead. Always check this with the known earth's magnetic field ($\sim 50 \mu\text{T}$), where the maximum positive direction is $\sim 60^\circ$ down from the geographic south (magnetic north) in the Netherlands. Fluxgate # 1267 was not modified and should be used as reference for correct positive field direction.

The 'zero'-field measurement shows the remnant field of the Kelvinox II cryostat, which is mainly shielded by a μ -metal cylinder, see Figure 54 for the exponential fit to the measured

absolute field in z-direction. Where the depth is given relative to the top of the opened cryostat.

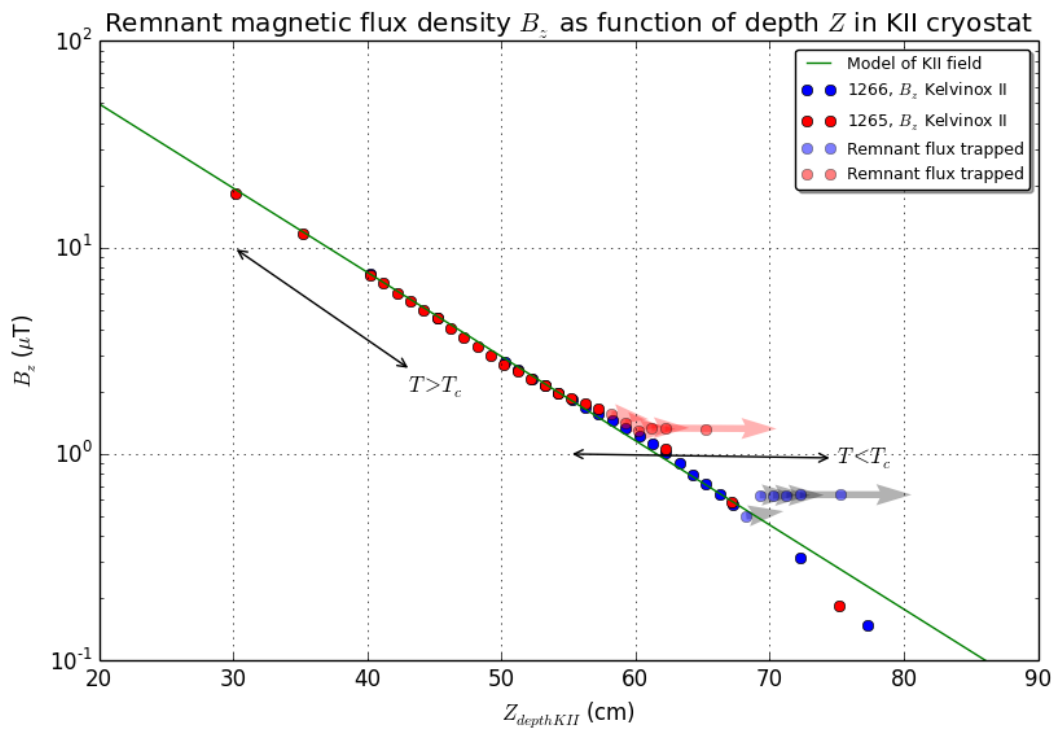


Figure 54. Measured magnetic flux density $|B_z|$ as a function of depth inside the Kelvinox II cryostat.

Also several hysteresis loops were measured where as long as $T < T_c$ at the part of the shield next to the fluxgate sensors the magnetic field was unchangeable by external fields. The bottom fluxgate showed a hysteresis (constant over depth) before the top fluxgate, suggesting that the bottom half of the shield was cooled below T_c at ~ 2 cm in depth before the top half, for 3 measurements.

An applied field with the solenoid has been ($\sim 100\%$) trapped during the superconductivity transition at T_c , as there would be a hysteresis for the measured flux density as a function of depth until the Nb wall next to the fluxgate sensor would become normal (non-superconductive) at $T > T_c$. See Figure 55 for the measurements that indicate the trapping of an applied magnetic field, notice that for a current $I_{sol} = 0.0$ mA a magnetic flux density of the same magnitude as for $I_{sol} = 5.0$ mA is measured as long as $T < T_c$.

Magnetic flux density B_z hysteresis loop as function of depth Z in KII cryostat

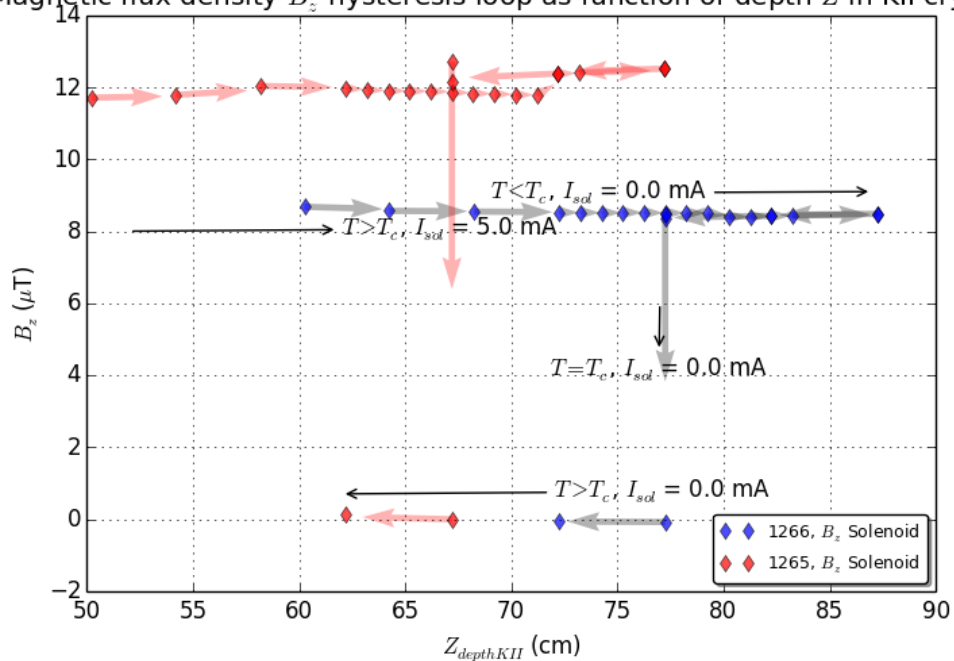


Figure 55. Flux density (remnant flux corrected) B_z as a function of depth Z , temperature T and current I .

The path in the plot of Figure 55 where hysteresis along Z can be seen is from $80 \rightarrow 87 \rightarrow 77$ cm, turning off the solenoid current didn't influence the measured value at the fluxgate positions.

A factor 4 decreased flux density from fluxgate # 1266 to # 1265 was found ($B_{1266} = 57$ nT, $B_{1265} = 14$ nT \pm 2 nT), if the remnant flux density was actively cancelled by the solenoid coil at the bottom sensor and top sensor during the transition into superconductivity. This is path is plotted in Figure 56. Which possibly is an indication that the phase transition (into Meissner state) can move from the bottom upward during the cooling. A second attempt resulted in a smaller residual B_z at both fluxgates, but in opposite polarity ($B_{1266} = +14$ nT, $B_{1265} = -20$ nT \pm 2 nT).

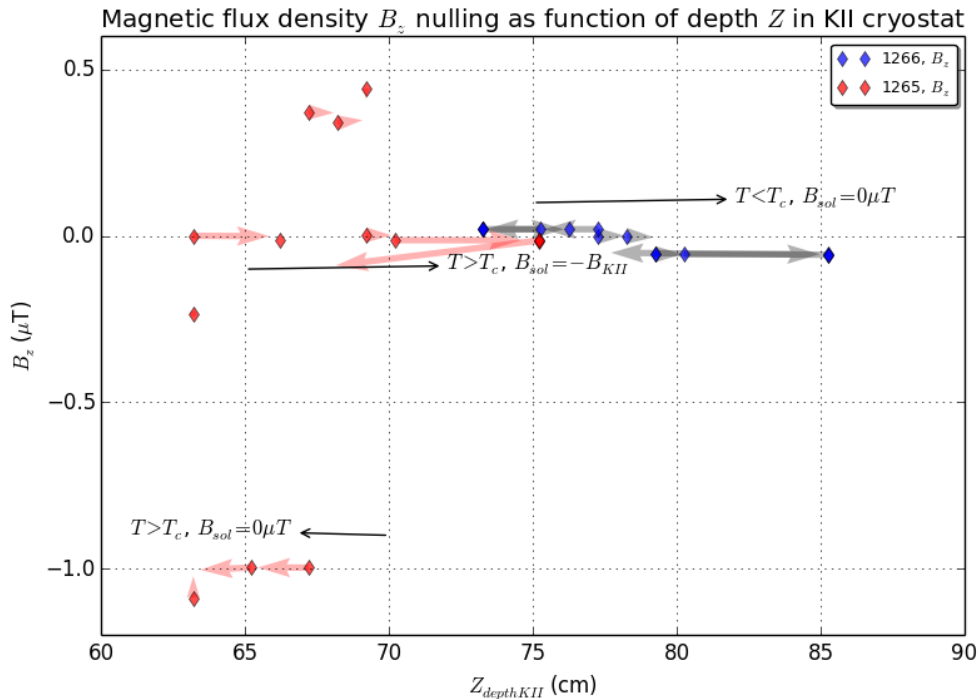


Figure 56. Active magnetic field nulled transition, where fluxgate # 1266 went through T_c before # 1265.

For the first attempt assuming an unidirectional field inside the shield, the ratio in measured flux densities agrees with the expected ratio for a controlled (bottom upward) cooled single body superconductor. The second attempt doesn't agree with the expected ratio, as there must be an n-polar (e.g. quadrupole) field to explain the opposite polarity in field direction. This possibly indicates that there is a flux trapped in the Nb shield between the 100 and 50 mm diameter parts.

! suggested ! use heaters on the 100 mm diameter shield part, this will prevent this edge from cooling below T_c before the bottom plate does. ! credits Pourya.

Heated phase transition measurements haven't shown improved flux expulsion from the shield. Result is presented in Figure 57, here the solenoid current was switched on and off at 92 cm depth. The upper shield part again went through T_c ~2 cm in depth after the lower part, this happened whilst the solenoid current was still off (0.0 mA). When cooling the top part an increase was seen in the measured flux density from 92 → 100 cm, this indicates the trapping and confining of magnetic flux in the shield itself.

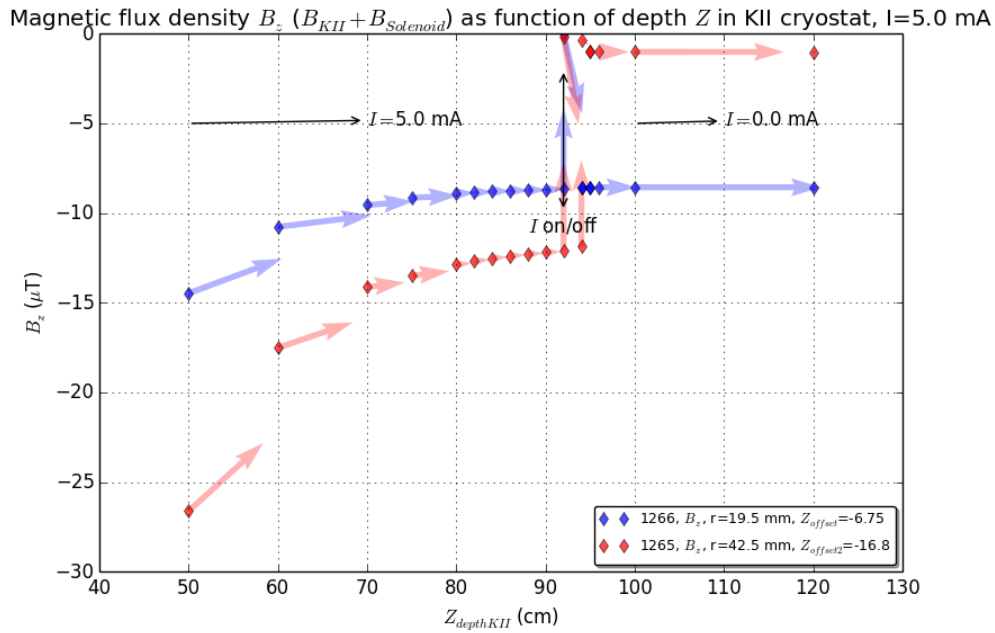


Figure 57. Measured (KII remnant + solenoid) magnetic flux density as a function of depth of measurement setup bottom below KII valve.

8.13 Point Cooled Phase-transition Experiment

Using modified setup with copper rod as thermal conductor to control cooling. Here the suggested in-field cooling technique was attempted for proof of concept.

8.13.1 Method

The same method is used as previous phase-transition measurement (see 8.12), the Nb shield is cooled in the remnant magnetic field of the Kelvinox II cryostat. Here the quality of the cooling is improved by cooling the Nb shield from a single 'point' on the bottom. To do this a copper rod is used as thermal conductor between the liquid He and the Nb shield. When the Nb shield cools through T_c there is an expected decrease in trapped magnetic flux relative to the applied magnetic flux, due to the Meissner phase expanding from a single point. Only if the temperature gradient is high enough to push out a part the vortices from the mixed Meissner state this should be observed. The temperature gradient is expected to increase by the copper rod modification.

By repeating the measurement in a magnetic flux generated by the solenoid and/or by cooling from space temperature instead of room temperature, the effect of $\frac{\delta T}{\delta Z}$ and $|B|$ on the expelled fraction can be investigated.

8.13.2 Result

In Figure 58 a hysteresis or insensitivity for B_z as a function of Z_{KII} after a step drop in measured flux at $Z_{KII} = 77 \pm .5$ cm was observed from $B_{KII}(77 \text{ cm}) = -138 \pm 5$ nT. This drop indicates the expulsion of all magnetic flux from the bottom part of the shield, due to the Meissner effect. After this drop an increase in opposite z-direction was observed to $B_{1266} = 31 \pm 2$ nT, that remained at this value until heating the sample completely above T_c .

Here fluxgate 1266 was positioned at 6.75 cm and 1265 at 16.8 cm from the bottom of the setup, the measured depth corrected for these Z offsets is used for the data points in Figure 58.

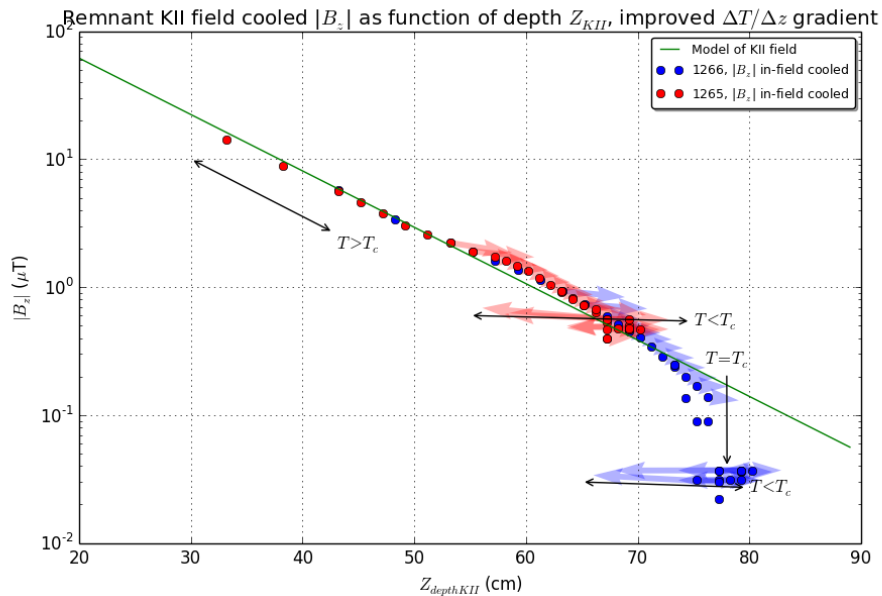


Figure 58. In-field cooled measurement data, with annotated temperature dependent hysteresis in depth.

Although several attempts were made to have the flux expelled from the upper shield part as well, it was observed that the remnant field for the depth of fluxgate #1265 was trapped repeatedly. This is a strong indicator of the presence of a flux trap between the narrow/lower and broader/higher part of the shield sample. Possibly caused by the curve/corners in profile, or the presence of a too low temperature gradient for expulsion of all the flux vortices.

Repeated measurements with higher flux density and/or lower temperature gradient ($T @ 20$ cm above liquid He $\rightarrow T_c$). In Figure 59 the result of a single measurement (only the bottom fluxgate) is given to illustrate the effect of point cooling the shield sample bottom.

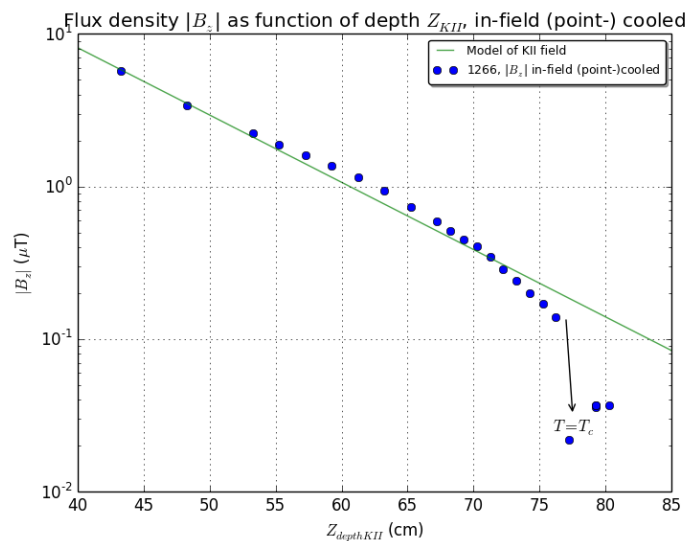


Figure 59. Resulting flux expulsion visible as a sudden decrease from expected remnant field (~ 100 nT).

9 Appendix C: Calibration parameters

In this chapter a list of calibrated or measured parameters are given for each experiment, also protocols* are given for working with the cryostat setup.

9.1 (cryo-)Solenoid

$B_0(I_{solenoid})$ plot, SQUID is in optimal rotated position.

The dimensional parameters of the used solenoid: $N = 411$, $L = 181 \text{ mm}$, $r = 61.5 \text{ mm}$, $Z_{offset} = 90.5 + ? + 35.0 - 16.0 = ?$.

In Figure 47 these parameters have been retrieved from fitting the $B(z)$ data from two series of measurements to the magnetic field amplitude model of a solenoid described by equation (8):

$$L_{fit} = 182 \pm 3 \text{ mm}, r_{fit} = 67 \pm 3 \text{ mm}, Z_{offset} = 74 \pm 2 \text{ mm}$$

9.2 '3D' SQUID probe/dipstick

Length: $1920 \pm 10 \text{ mm}$

Tip diameter: $22 \pm 1 \text{ mm}$ (Kapton tape applied to protect electronics)

SQUID height(from 0,0 reference): $35.25 \pm .3 \text{ mm}$

Name: SQUID(Magnicon 1) Type: C6WS (checked) (SQUIDviewer Save 3-9-2013 on PC)

$$\frac{1}{M_f} = 16.8 \mu\text{A}/\phi_0$$

SQUID area/sensitivity parameter: $S_\phi = 7 \text{ nT}/\phi_0 \pm 0.3\%$

Angle offset between laser alignment on connector box and SQUID's x-axis of 7.5° .

9.3 Fluxgate magnetometer

Unlike the dc-SQUID magnetometer the fluxgate is operable at room temperature as well as low temperatures. The directional calibration of this device is done by measuring what angle is the most sensitive direction relative to the exterior geometry.

The systematic error in the calibration setup could not be reduced to a value less than the 0.2° maximum case alignment offset specified in the Bartington Mag-01H manual, concluding that less than 2% of the transvers field component is measured in axial direction for the 3 cryo-fluxgate sensors.

The fluxgate sensor tips have a length of 32 mm with a 30 mm sensitive probe fixed inside, the cylindrical diameter of the probes varied as follows:

for #1265 $D_{var} = 5.8 \rightarrow 6.0 \text{ mm}$, #1266 $D = 6.0 \text{ mm}$, #1267 $D = 6.1 \text{ mm}$, all were measured within 0.05 mm accuracy.

9.4 Helmholtz Setup

Inside a set of 4 coils (2 pairs of Helmholtz coils) a relatively constant over area magnetic field can be applied along the axis between either Helmholtz coil, ideally the radius of both identical coils should be equal to the distance between the 2 coils .

$h_{b \rightarrow y} = 165 \pm .5$ mm, $r1 = 145.5 \pm .5$ mm (outer coils blue and yellow)

$h_{r \rightarrow g} = 142 \pm .5$ mm, $r2 = 125.25 \pm .5$ mm (inner coils red and green)

*all distances are given relative to the centres of the volumes of loops.

9.5 *Cooling down the Kelvinox II (cryostat)

The cryostat Kelvinox II is a thermally isolated volume where cryogenic experiments can be carried out at liquid nitrogen or liquid helium temperatures. To get the Dewar to hold an amount of liquid He (at $T = 4.2$ K) a cooling process has to be followed step by step.

1. Create a vacuum in the vacuum chamber that thermally isolates the Dewar.
2. Cool the Dewar to $T = 80$ K by pouring in liquid Nitrogen.
3. Flush all liquid Nitrogen out with high pressure He gas, a tube from the bottom of Dewar drains any liquid Nitrogen out. (If there is some residual liquid Nitrogen, the liquid He will lose all its cooling capacity by creating solid Nitrogen (ice at $T < 63$ K) and is lost to the return as He gas.
4. Cool the Dewar down to 4K with liquid He, by pouring this in via a thermally isolated pipe/tube.

9.6 *Placing the Insert (holder for the probe) with sliding seal

The Insert is a mount for the solenoid and the niobium shield where the dipstick with SQUID is lowered into. Depending on what needs to be measured or calibrated, components like the solenoid and niobium shield can be added or removed.

To have a 0,0 mm depth measurement (z-axis direction) an aluminium plate is mounted exactly 35 mm below the plate holding the solenoid. The solenoid cylinder is 200 mm long and can contain the niobium shield.

An overview of the Insert with placement of the Probe inside is given in Figure 18, where the marked heights (mm) are reference distances along the z-axis with 0.0 mm defined at the top surface of the bottom plate.

9.7 *Lowering dipstick with rotatable SQUID

The SQUID itself is mounted on the end of a long narrow dipstick which fits into the Insert. This dipstick is 'dipped' into the liquid helium by inserting it in the opening of the Insert. This allows the SQUID to be rotated around the x- and z-axes, also the height (distance along z-axis) from the bottom plate of the Insert can be varied.

-
- ⁱ Official SRON website: <http://www.sron.nl/mission-and-strategy-about-sron-595.html>
- ⁱⁱ Official JAXA website: http://www.ir.isas.jaxa.jp/SPICA/SPICA_HP/mission-en.html
- ⁱⁱⁱ R.A. Hijmering, P. Khosropanah, M. Ridder, J.R. Gao, M. Lindeman, H. Hoovers, J. van der Kuur, L. Gottardi, B. Jackson, R. Huiting, M. van Litsenburg, 'Effects of Magnetic Fields on Highly Sensitive TiAu TES Bolometers', (<http://resolver.tudelft.nl/uuid:516c9963-4a87-4469-ae4d-5da5e2132f2e>)
- ^{iv} C. Kittel, (2004), *Introduction to Solid State Physics*. John Wiley & Sons. pp. 273–278. (ISBN 978-0-471-41526-8)
- ^v C. Benvenuti et al, 'MAGNETIC FLUX TRAPPING IN SUPERCONDUCTING NIOBIUM', from CERN 1997 Workshop on RF Superconductivity.
- ^{vi} J.D. McCambridge, 'The Superconducting Properties of Niobium-Titanium Alloy Multilayers', (<http://www.yale.edu/proberlab/Papers/McCambridgeDissertation.pdf>).
- ^{vii} H.R. Kercher, 'Critical fields H_c and H_{c2} of superconducting niobium', (http://prb.aps.org/pdf/PRB/v24/i3/p1200_1).
- ^{viii} P.E. Goa, 'Real-time magneto-optical imaging of vortices in superconducting NbSe₂', (<http://www.mn.uio.no/fysikk/english/research/groups/amks/superconductivity/files/sv.pdf>).
- ^{ix} T. Golüke, 'The influence of remanence and flux trapping on the magnetic shielding properties of mu-metals and superconductors' (<http://essay.utwente.nl/63720/>).
- ^x N. S. Alzayed, 'Magnetic Attenuation by HTC Superconducting Cylinders'
- ^{xi} H.J. van Weers, C. Bruineman, G. Muckus, 'Cryogenic Magnetic Shield Modeling & Verification'.
- ^{xii} R. L. Peterson, 'Sinusoidal Response of dc SQUIDs For rf Power Measurements'
- ^{xiii} O.V. Lounasma, 'Experimental Principles and Methods Below 1K', ISBN: 0-12-455950-6
- ^{xiv} R. M. Bozorth, 'Ferromagnetism', ISBN: 0-7803-1032-2
- ^{xv} J. Clarke, A.I. Braginsky, 'The SQUID Handbook: Fundamentals and Technology...', ISBN: 978-3-527-60458-6